Mineral-melt vanadium oxybarometry for primitive arc magmas: effect of hydrous melt composition on fO2 estimates

Saskia Erdmann, Michel Pichavant, Fabrice Gaillard

Mineral-melt vanadium oxybarometry for primitive arc magmas: Effect of hydrous melt composition on fO_2 estimates

Submitted for publication to Contributions to Mineralogy and Petrology

Saskia Erdmann*[1], Michel Pichavant[1], Fabrice Gaillard[1]

(1) Université Orléans, CNRS, BRGM, ISTO, UMR 7327, 45071 Orléans, France

*Corresponding author. Email: saskia.erdmann@cnrs-orleans.fr; ORCID: 0000-0002-1083-9251

Keywords: Vanadium, oxybarometry, temperature, melt H_2O, primitive arc magma, St. Vincent

AUTHOR CONTRIBUTIONS

All authors contributed to the study conception. Samples were provided by Michel Pichavant. Data collection and analysis were performed by Saskia Erdmann. Data interpretation involved all authors. The draft of the manuscript was written by Saskia Erdmann, while Michel Pichavant and Fabrice Gaillard commented on all versions of the manuscript.

STATEMENTS AND DECLARATIONS

The authors have no relevant financial or non-financial interests to disclose

ABSTRACT

If primitive arc magmas are primarily oxidized or if they acquire their oxidizing character during crustal evolution remains debated. Mineral-melt V partitioning is extremely redox sensitive and has the potential to resolve this debate, but critical low-temperature, hydrous experimental partitioning data are limited. We present new experimental V partitioning data for olivine-melt, spinel-melt, and clinopyroxene-melt based on the ≤1200 °C, hydrous basalt phase equilibrium experiments of Pichavant et al. (2002) and Pichavant & Macdonald (2007). Combined with published experimental data, we use our olivine-melt V partitioning coefficients to show that – contrary to previous conclusions – hydrous melt composition, i.e. melt H_2O concentration in addition to the concentration of other melt components, affects V partitioning and thus calculated fO_2, systematically overestimating fO_2 for olivine-melt equilibrated at high melt H_2O concentration. False absolute fO_2 values and false oxidation or reduction trends may be inferred. Based on these findings, we have calibrated a set of new olivine-melt oxybarometers applicable to hydrous arc magmas partially crystallized at ~1025-1350 °C. In a case study on a high-Mg basalt from St. Vincent, Lesser Antilles, we show that olivine-melt V oxybarometry records oxidizing near-liquidus conditions (~QFM+1.8) and possibly limited oxidation (~0.3 log units) during intermittent crustal magma storage.

INTRODUCTION

Most arc magmas are more oxidized than mid-ocean ridge magmas, but it remains debated if their more oxidized character derives from oxidized primary melts or if it results from differentiation at crustal level (Canil 2002; Lee et al. 2005; Mallmann & O'Neill 2009; Kelley & Cottrell 2012; Brounce et al. 2014; Laubier et al. 2014; Grocke et al. 2016; Prytulak et al. 2017; Ulmer et al. 2018; Tang et al. 2018, 2019; Bucholz & Kelemen 2019; Wang et al. 2019). Several whole-rock geochemical models (for V/Sc, Eu/Eu*, Zn/Fe) as well as phase equilibrium experiments have been used to suggest that the majority of mantle-derived magmas initially has an oxygen fugacity (fO_2) near the quartz-fayalite-magnetite (QFM) buffer, regardless of their geodynamic origin, and that more oxidized conditions are acquired through fractionation, crustal assimilation, or degassing (e.g., Lee et al. 2005; Mallmann & O'Neill 2009; Ulmer et al. 2018; Tang et al. 2018, 2019). Most mineral-melt oxybarometry, experimental and recent whole-rock geochemical modelling studies, in contrast, support the notion that primitive mantle-derived magmas have variable fO_2, where primitive arc magmas are generally more oxidized (commonly ~QFM+0.5 to QFM+3.5) than primitive mid-ocean ridge magmas (commonly ~QFM±0.5) (e.g., Carmichael 1991; Pichavant & Macdonald 2007; Kelley & Cottrell 2012; Brounce et al. 2014; Gaillard et al. 2015; Bucholz & Kelemen 2019). Oxidation of primitive arc magmas through fractionation, crustal assimilation, or degassing is not ruled out, but invoked to be superimposed on relatively oxidized primary melts.

Consensus exists in that accurately constraining the fO_2 of primary magmas and their possible redox evolution is critical for resolving the debate and for improving our understanding of Earth's redox reservoirs through time. Vanadium partitioning between minerals and melts is known to be extremely redox sensitive, particularly between ~QFM-5 and QFM+5 (Canil 2002; Lee et al. 2005; Mallmann & O'Neill 2009) and thus over a large fO_2 range that covers most estimated

terrestrial magma redox conditions (Gaillard et al. 2015; Righter et al. 2020). A number of mineral-melt V oxybarometers exists for olivine, clinopyroxene, and spinel (Canil & Fedotchouk 2001; Mallmann & O'Neill 2013; Shishkina et al. 2018; Wang et al. 2019), which are increasingly applied, given that V compositions can be easily and rapidly acquired by laser ablation inductively coupled plasma mass spectrometry and for some minerals by electron microprobe. Existing experimental V mineral-melt partitioning data are, however, biased towards high-temperature, anhydrous equilibria. To date, few experimental studies – those of Laubier et al. (2014), Shishkina et al. (2018), and Wang et al. (2019) – have systematically characterized V mineral-melt partitioning at relatively low temperatures (≤1200 °C) for compositions approaching those of primitive arc magmas and at anhydrous to hydrous conditions. To add to the limited database, we have acquired new partitioning data for olivine-melt, clinopyroxene-melt, and spinel-melt for hydrous, 1050-1200 °C basalt phase equilibrium experiments of Pichavant et al. (2002) and Pichavant & Macdonald (2007). Using our and published data, we first test the recent V olivine-melt, clinopyroxene-melt, and spinel-melt oxybarometers of Mallmann & O'Neill (2013), Shishkina et al. (2018), and Wang et al. (2019) and then derive a new set of olivine-melt V oxybarometers for arc magmas, which we apply to constrain fO_2 and its evolution for a primitive, high-Mg magma from St. Vincent, Lesser Antilles.

METHODS BACKGROUND

Vanadium can occur in valence states V^0, V^{2+}, V^{3+}, V^{4+}, or V^{5+} (Sutton et al. 2005; Wood et al. 2008), with V^{3+} and V^{4+} being the dominant species at terrestrial magma redox conditions (Canil 1997; Lee et al. 2005; Mallmann & O'Neill 2009). In olivine, clinopyroxene, and spinel, V^{3+} is significantly more compatible than V^{4+} (e.g., Canil 1997; Righter et al. 2006; Mallmann & O'Neill

2009; Shishkina et al. 2018; Wang et al. 2019), and olivine/clinopyroxene/spinel-melt V partitioning coefficients therefore strongly decrease with increasing oxidation state, while other intensive parameters also have a minor, but nevertheless relevant effect on mineral-melt V partitioning. Olivine-melt V partitioning coefficients are inferred to increase with decreasing temperature, increasing olivine forsterite content, increasing proportions of melt network formers SiO_2 and Al_2O_3 relative to network modifiers CaO, Na_2O, and K_2O, or decreasing anhydrous melt NBO/T (i.e. the ratio of non-bridging oxygen to tetrahedral cations in the melt) (Mallmann & O'Neill 2013; Wang et al. 2019). Pressure and melt H_2O concentration, in contrast, have been inferred to have no significant effect on V olivine-melt partitioning (Canil & Fedortchouck 2001; Shishkina et al. 2018; Wang et al. 2019). Vanadium partitioning coefficients for clinopyroxene-melt and spinel-melt are inferred to also increase with decreasing temperature and to vary with mineral and melt composition, which in turn are controlled by other variables including pressure (Horn et al. 1994; Toplis & Corgne 2002; Wang et al. 2019; Holycross & Cottrell 2022).

The olivine-melt V oxybarometer of Mallmann & O'Neill (2013) has been calibrated for a large fO_2 range (~QFM-4 to QFM+4), but at high temperature (1200-1530 °C) and anhydrous, atmospheric conditions. Effects of temperature, olivine forsterite content, and melt SiO_2, Al_2O_3, CaO, Na_2O, and K_2O in addition to fO_2 on V partitioning are considered in the calibration, which has an estimated uncertainty of ~0.5 log units at 2σ level. The olivine-melt V oxybarometer of Wang et al. (2019) has also been calibrated for a large fO_2 range (~QFM-4 to QFM+4) and at relatively high temperature (1150-1470 °C), yet for anhydrous to hydrous, low- to high-pressure conditions. Effects of temperature and anhydrous NBO/T in addition to fO_2 on V partitioning are considered in the calibration with an apparent uncertainty of ~0.5 log units at 2σ level (cf. their Fig. S5). The olivine-melt V oxybarometer of Shishkina et al (2018) (equation 4) has been

111 calibrated for primitive arc magmas crystallized at ≤1250 °C and at hydrous to anhydrous, low- to
112 intermediate-pressure conditions and for a relatively large fO_2 range (~QFM-2 to QFM+3). Effects
113 of intensive parameters in addition to fO_2 on olivine-melt V partitioning were not ruled out, but
114 considered insignificant for the calibration range. The uncertainty of the oxybarometer is estimated
115 to increase with decreasing V partitioning coefficient (given that V concentrations in olivine
116 decrease and analytical uncertainties thus increase), ranging between ~0.5 and 1.0 log units at 2σ
117 level. The clinopyroxene-melt and spinel-melt V oxybarometers of Wang et al. (2019) have been
118 calibrated for the same fO_2 range (~QFM-4 to QFM+4) as their olivine-melt oxybarometer, also at
119 high temperature (~1150-1350 °C) and at anhydrous to hydrous, low- to high-pressure conditions.
120 Effects of temperature and tetrahedral Al (for clinopyroxene) or Cr number (for spinel) in addition
121 to fO_2 on V partitioning are considered in the calibrations, which have apparent uncertainties of
122 ~0.5 log units at 2σ level (cf. their Fig. S5).

123

124 **GEOLOGICAL BACKGROUND**

125 Primitive high-Mg basaltic magmas (i.e. primary or near-primary mantle-derived melts) erupt in
126 arcs, but they are not commonplace (e.g. Grove et al. 2012), with some exceptions including the
127 southern section of the Lesser Antilles arc. The Lesser Antilles arc is a mature ocean-ocean
128 subduction zones that extends for ~750 km, resulting from the westward subduction of the Atlantic
129 beneath the Caribbean Plate, which has been active since the early Miocene, following earlier
130 subduction systems in the eastern Caribbean (Macdonald et al. 2000; Evain et al. 2013; Allen et al.
131 2019). It comprises the islands of Saba, Statia, St. Kitts, Nevis, Montserrat, Guadeloupe, Dominica,
132 Martinique, St. Lucia, St. Vincent, the Grenadines, and Grenada, which all have active or
133 potentially active volcanic centres. A wide range of magma types have erupted, ranging from low-

134 K tholeiites over calc-alkaline basalts to alkalic basalts. The primitive, high-Mg basalts have mostly
135 erupted on St. Vincent, the Grenadines and Grenada, which are interpreted as parental magmas of
136 low-Mg, high-Al basalts and other more evolved magmas of the arc (Heath et al. 1998; Macdonald
137 et al. 2000; Pichavant & Macdonald 2007; Melekhova et al. 2015). They provide an opportunity to
138 study the fO_2 and other intensive parameters of mantle-derived magmas that have been largely
139 unaffected by fractionation or contamination at crustal level.

140 The island of St. Vincent, from which the sample of our study derives, is dominated by
141 Soufriere volcano in the northern part of the island, which is largely composed of calc-alkaline
142 basalts and basaltic andesites (Heath et al., 1998). Its early activity (~0.6 Ma-10 ka) was dominated
143 by the eruption of basaltic and basaltic andesitic lavas, the so-called Pre-Somma lavas. Later
144 activity produced the Yellow Tuff Formation (black scoria to yellow lapilli and tuff; 3600-4500
145 years bp), the Crater Lava Formation (ponded basaltic and basaltic andesitic lavas), and the
146 Pyroclastic Formation (succession of pyroclastic fall and flow deposits) with at least five major
147 historic eruptions. Sample STV301 of Heath et al. (1998), which we have used, is a high-Mg basalt
148 that derives from the Pre-Somma unit sampled at Black Point (13°15.65'N, 61°07.05'W). High-
149 Mg basalt STV301 and other high-Mg basalts from the southern part of the arc are inferred to
150 represent slightly enriched, near-primary hydrous mantle melts, which have last equilibrated with
151 peridotite at ~1130-1240°C and ~11-17 GPa (Heath et al. 1998; Pichavant et al. 2002; Bouvier et
152 al. 2008; Melekhova et al. 2015). Experimental studies and olivine-spinel oxybarometry have
153 inferred an oxidized redox state with an fO_2 of ~QFM+0.9 to ~QFM+2.6 for the primitive St.
154 Vincent magmas (Heath et al. 1998; Macdonald et al. 2000; Pichavant et al. 2002; Pichavant &
155 Macdonald 2007), which is within the range of fO_2 conditions (~QFM+0.5 to +3.5) typically
156 inferred for arc magmas using petrological methods (e.g., Carmichael 1991; Kelley & Cottrell

157 2012; Brounce et al. 2014; Gaillard et al. 2015; Bucholz & Kelemen 2019). Melt H_2O
158 concentrations of high-Mg basalts from St. Vincent, including STV301, are inferred to have been
159 ~5 wt% (Pichavant & Macdonald 2007; Bouvier et al. 2008). Melt CO_2 concentrations and thus
160 direct constraints on melt volatile saturation remain unconstrained for the Pre-Somma lavas, but
161 are high (up to >3000 ppm CO_2) for dacitic melt inclusions from basaltic andesites erupted in 1477
162 and 1902 AD at St. Vincent (Balcone-Boissard et al. 2023). Some originally volatile-undersaturated
163 high-Mg basalts may have fractionated to high-Al basalts and more evolved magma with ~7-8 wt%
164 H_2O (Pichavant & Macdonald 2007; Balcone-Boissard et al. 2023), but most St. Vincent and Lesser
165 Antilles melt inclusion H_2O and K_2O compositions show no or negative correlation (Bouvier et al.
166 2008; Balcone-Boissard et al. 2023), which indicates degassing-driven crystallization and thus
167 volatile saturation during partial crystallization at crustal level.

168

169 **SAMPLES, METHODS, NEW DATA**

170 We have investigated the natural STV301 high-Mg basalt in one thin section and selected run
171 products of phase equilibrium experiments of Pichavant et al. (2002) and Pichavant & Macdonald
172 (2007) that have used STV301 as the starting material. The experimental run products of Pichavant
173 et al. (2002) and Pichavant & Macdonald (2007) were all considered for our study, but only phases
174 from a subset of eleven charges were feasible for trace-element analysis by laser ablation
175 inductively coupled plasma mass spectrometry (LA-ICP-MS). Eight of the charges were partially
176 crystallized in internally heated pressure vessels (IHPV; experiments of Pichavant & Macdonald
177 2007), whereas three of the charges were partially crystallized in piston cylinder presses (PC;
178 experiments of Pichavant et al. 2002). The experiments were performed at conditions ranging from
179 ~QFM+0.7 to ~QFM+3.1, ~1050 to ~1200 °C, and ~400 to 1450 MPa, where melt H_2O

concentration varied between ~2.3 and 7.7 wt% (Table 1). Details on the control of the experimental intensive parameters are provided below, in the supplementary text, and in the publications of Pichavant et al. (2002) and Pichavant & Macdonald (2007).

All samples were imaged in backscatter-electron mode using a ZEISS Merlin Compact SEM at the Institut des Sciences de la Terre d'Orléans (ISTO-CNRS-Université d'Orléans-BRGM), France. Phase proportions of the natural sample were determined by point-counting (this study), while phase proportions of the experimental run products have been previously determined by mass balance (Pichavant et al. 2002 and Pichavant & Macdonald 2007). For the experimental samples, we have used the major- and minor-element phase compositions reported by Pichavant et al. (2002) and Pichavant & Macdonald (2007). For the natural sample, we have determined new major- and minor-element compositions for olivine, spinel, clinopyroxene, and matrix using a Cameca SX five electron microprobe in wavelength dispersive mode (details are provided in the supplementary text). The redox-sensitive V concentrations of olivine, spinel, clinopyroxene, and glass/matrix were determined for the natural and the experimental samples using LA-ICP-MS. Temperature-sensitive concentrations of Sc, Y, and Ni were also determined for all phases by LA-ICP-MS. For the experimental samples, the data showed zoning in Sc for some olivine (equilibrated at low-temperature) and contamination problems for Ni and Y for other charges (equilibrated in PCs). Given these problems, we report the experimental Sc, Y, and Ni data only in the supplementary text, figures, and Table S1. For the natural samples, the Sc, Y, and Ni concentrations are reported in the main text, which we use to interpret and to quantify crystallization conditions. The four elements of interest (V, Sc, Y, Ni) as well as Si and Al as internal standards were measured as masses ^{27}Al, ^{29}Si, ^{45}Sc, ^{51}V, ^{60}Ni, and ^{89}Y using a RESOlution SE ArF excimer laser ablation system coupled to an Agilent 8900 QQQ mass spectrometer. Instrument parameters were set to

common conditions, and calibration and acquisition followed established procedures, which are outlined in the supplementary text and in Table S1. Phase compositions were determined by point analyses, while zoning was evaluated by LA-ICP-MS compositional mapping. Raw LA-ICPMS data were reduced using Glitter (point analyses; version 4.4.4; van Achterbergh et al. 2000) and Iolite (compositional maps; version 4.7.1; Paton et al. 2011; Petrus et al. 2017). Accuracy and precision determined for V, Sc, Y, and Ni concentrations in BCR-2G, BHVO-2G, and BIR-1G reference materials were mostly better than 15 and 5%, respectively (Table S2).

OXYBAROMETER TEST AND CALIBRATION DATA

Our aim was to test how the recent olivine-melt V oxybarometers of Mallmann & O'Neill (2013), Shishkina et al. (2018) (equation 4), and Wang et al. (2019) as well as the clinopyroxene-melt and spinel-melt V oxybarometers of Wang et al. (2019) perform for primitive, hydrous arc magmas and to improve on them if possible. We have therefore focused on mineral-melt V partitioning coefficients determined for experiments performed at hydrous conditions and low temperatures with starting material compositions approaching those of primitive arc magmas, but we have also integrated relevant anhydrous V partitioning data (Fig. 1). In addition to our new data presented below, we have considered the experimental studies of Laubier et al. (2014), Shishkina et al. (2018), and Wang et al. (2019), for which a close approach to equilibrium was inferred in the original publications (to which the reader is referred for details). However, to consider only the highest quality data, we have selected a subset of the published data (1) from experiments with estimated melt H_2O concentrations of <10 wt% (which can be quenched to a homogeneous glass); and (2) from experiments with ≤±20% Fe loss/gain (which can be assumed to have approached chemical and fO_2 equilibrium), which excluded data from 17 experiments of Wang et al. (2019).

226 The hydrous partitioning coefficients of Shishkina et al. (2018), Wang et al. (2019), and our
227 new data were supplemented by anhydrous, low-temperature V partitioning data from Laubier et
228 al. (2014) for the same fO_2 range and similar starting material compositions. This selection yielded
229 a anhydrous to hydrous partitioning dataset equilibrated at an fO_2 of ~ΔQFM-2.0 to ~ΔQFM+4.0,
230 at melt H_2O concentrations of 0-9.5 wt%, and at temperatures of 1025-1350 °C but mostly 1025-
231 1200 °C (Fig. 1) with 54 partitioning coefficients for olivine-melt (Table S4), 13 partitioning
232 coefficients for spinel-melt (Table S5) and 11 partitioning coefficients for clinopyroxene-melt
233 (Table S6). Vanadium partitioning data determined at higher temperatures or for compositions that
234 strongly deviate from the composition of primitive arc magmas (e.g., those of Canil &
235 Fedortchouck 2001; Toplis & Corgne 2002; Papike et al. 2013; Mallmann & O'Neill 2009, 2013;
236 Holycross & Cottrell 2022) were not used. The fO_2 conditions of the considered studies were
237 variably expressed in log units or relative to various QFM or NNO buffer calibrations, which we
238 have recalculated relative to the QFM buffer of O'Neill (1987) (Tables S4-S6).

239 Our focus on hydrous partitioning data for arc-type magma compositions is different from
240 the approach taken by Shishkina et al. (2018) and Wang et al. (2019) for their V oxybarometers for
241 arc magmas, who have integrated limited hydrous olivine-melt V partitioning data (n=12 or n=26)
242 with anhydrous partitioning data (n=47 or n=169) from experiments extending over a larger
243 temperature range and also a larger compositional range than the hydrous equivalents (Fig. 1). We
244 posit that focusing our dataset on hydrous to anhydrous V partitioning data for compositions,
245 temperatures (~1025-1350 °C), and fO_2 conditions (~QFM-2 to QFM+4) relevant to partial
246 crystallization of most primitive arc magmas (Carmichael 1991; Grove et al. 2012; Kelley &
247 Cottrell 2012; Brounce et al. 2014; Gaillard et al. 2015; Bucholz & Kelemen 2019) permits us to

248 best assess relevant effects of their various intensive parameters on V partitioning and thus on fO_2
249 estimates.

250

251 **EXPERIMENTAL fO_2 AND MELT H_2O CONSTRAINTS**

252 For atmospheric pressure experiments in gas mixing furnaces (i.e. for the considered experiments
253 of Laubier et al. 2014), control of intensive parameters is relatively straightforward with melt H_2O
254 concentrations of <0.1 wt% and an accuracy of better than ±0.1 log units for fO_2. For high-pressure
255 experiments, fO_2 and melt H_2O concentration are more difficult to maintain and to determine, given
256 that the systems are partly open. Oxygen fugacity may be imposed through pressurizing gas
257 mixtures (commonly Ar-H_2), experimental assemblies, double-capsule buffer techniques, and fluid
258 concentrations (H_2O-CO_2) in individual charges. The fO_2 imposed by gas mixtures may be directly
259 measured by Shaw membrane (experiments of Shishkina et al. (2018)), but is more commonly
260 determined using solid buffer capsules or redox-sensitive run products (experiments of Pichavant
261 et al. (2002), Pichavant & Macdonald (2007), and Wang et al. (2019). For experiments in internally
262 heated pressure vessels (experiments of Pichavant & Macdonald (2007) and Shishkina et al. (2018))
263 and piston cylinder presses (experiments of Pichavant et al. (2002) and Wang et al. (2019)),
264 experimental fO_2 is typically constrained with accuracies of better than ~±0.3 to 0.5 and ~±0.5 to
265 1.0 log units, respectively. Melt H_2O concentrations can be constrained by various techniques, but
266 only indirectly, i.e. for the quenched glasses. Water concentrations measured by secondary ion
267 mass spectrometry (some data from Pichavant et al. (2002) and Pichavant & Macdonald (2007)) or
268 Fourier-transform infrared spectroscopy (some data of Shishkina et al. (2019)) are in most cases
269 accurate to within ±0.5 wt%, whereas melt H_2O concentrations inferred on the basis of saturation
270 models are typically within ±0.5-1.0 wt% (some data of Shishkina et al. (2019)). Melt H_2O

concentrations calculated by difference from electron microprobe totals (some data from Pichavant et al. (2002) and Pichavant & Macdonald (2007) and all data from Wang et al. (2019)) have accuracies of ideally ~±1.0 wt% (Devine et al. 1995) but may overestimate concentrations by up to ~+2 wt% (Hughes et al. 2019) or more (e.g. Holycross & Cottrell (2022), especially for high melt H_2O concentrations. These uncertainties are indicated and considered below; further details are provided in the published experimental studies of Pichavant et al. (2002), Pichavant & Macdonald (2007), Laubier et al. (2014), Shishkina et al. (2018), and Wang et al. (2019).

STUDY OUTLINE

We first present a textural-compositional characterization of olivine, spinel, clinopyroxene and glass of the STV301 phase equilibrium experiments of Pichavant et al. (2002) and Pichavant & Macdonald (2007). Together with the selected literature data (Tables S3 to S5), we then use our compositions to evaluate (1) the olivine-melt V oxybarometers of Mallmann & O'Neill (2013), Shishkina et al. (2018) (equation 4), and Wang et al. (2019); and (2) the spinel-melt and clinopyroxene-melt V oxybarometers of Wang et al. (2019). Following the evaluation, we formulate a set of new olivine-melt V oxybarometers for hydrous arc magmas partially crystallized at ~1050-1350 °C, which we then apply in a petrographic case study on the natural STV301 basalt from St. Vincent, in combination with all tested oxybarometers and the Sc/Y and Ni thermometers of Mallmann & O'Neill (2013) and Pu et al. (2017). A challenge for applying the mineral-melt V oxybarometers and thermometers to the natural STV301 sample was that a record of melt compositions in the form of glassy melt inclusions or glassy matrix is lacking. Possible crystallized melt inclusions (i.e. inclusions in 2D but not necessarily in 3D) large enough for LA-ICP-MS analysis are also rare, which precluded meaningful characterization, and we have therefore (1)

analyzed the crystallized matrix/groundmass of the natural sample and (2) estimated melt compositions as outlined later in the text.

RESULTS AND DISCUSSION

Experimental constraints

Phase relations and compositions

The STV301 experimental run products – which have been previously characterized by Pichavant et al. (2002) and Pichavant & Macdonald (2007) in regards to their assemblage, textures, and major- and minor-element phase compositions – comprise olivine-spinel-glass, olivine-spinel-clinopyroxene-glass, olivine-spinel-clinopyroxene-plagioclase-glass, or orthopyroxene-clinopyroxene-spinel-glass and quench crystals (Table 1; Fig. S1). Olivine, spinel, clinopyroxene, and glass were successfully analyzed by LA-ICP-MS in 9, 3, 2, and 12 charges, respectively (Table 1; Tables S4-S6). Olivine (~2-17 wt%) forms subhedral to euhedral crystals, which are up to ~100 μm but typically ~10-20 μm in size. Olivine crystals of the ≥1180 °C experiments are unzoned and largely inclusion-free (Fig. S2a-c). Olivine formed at ≤1090 °C, however, becomes partly zoned and has locally abundant small (<1-2 μm) spinel, glass, and/or fluid inclusions especially in crystal cores (Fig. S2d-i). Unzoned inclusion-free olivine cores and unzoned inclusion-free near-rim zones have low V concentrations (~1.7-12.7 ppm), which decrease with increasing fO_2 (Table 1). The inclusion-rich cores, in contrast, yield relatively V-rich compositions, representing mixtures of olivine±spinel±glass inclusion analyses, which we have removed from the dataset. The variation of V in olivine of individual charges is relatively low (mostly ~<15% 2RSDs; Table 1), indicating that inclusions were successfully eliminated from our data set.

316 Spinel (~1-2 wt%) in the experimental charges forms euhedral to subhedral crystals and
317 inclusions in olivine, which are commonly ≤10 μm in size (Fig. S2a). In all experimental run
318 products, some spinel crystals show core-rim zoning from BSE-bright cores to BSE-dark rims,
319 where zoning is sharp in the low-temperature, low-H_2O experiments and gradational in the high-
320 temperature, high-H_2O experiments. Cores of the zoned crystals were not analyzed, as they are
321 inherited from the starting material (cf. Pichavant et al. (2002) and Pichavant & Macdonald (2007);
322 Fig. S1a). Cores of the unzoned spinel crystals and near-rim zones of the zoned spinel crystals have
323 high V concentrations (~320-1080 ppm) which strongly decrease with increasing experimental fO_2
324 with limited variation in spinel of individual charges (≤25% 2RSDs) (Table 1). The experimental
325 clinopyroxene crystals (~6-25 wt%) are subhedral-euhedral, typically clustered in the experimental
326 charges, and commonly <5-10 μm large (Fig. S2g-i). They show no obvious core-rim zoning in
327 BSE images, but they were too small to assess trace-element zoning by LA-ICP-MS mapping. The
328 crystals have intermediate V (~130-450 ppm), showing limited variation in crystals within
329 individual charges (≤15% 2RSDs), but only few crystals were large enough for analysis (Table 1).

330 Glasses (~51-96 wt%) of the experimental run products are largely homogeneous in BSE
331 imaging mode, but commonly comprise quench crystals, especially those of the H_2O-rich
332 experimental charges (Fig. S2a,d,g). Glasses around quench crystals (Fig. S2a-f) and pyroxene
333 (Fig. S1b,c,d,f,j, S2g) show <5-10 μm wide, BSE-dark boundary layers, which were too narrow
334 for quantitative analysis (Fig. S2d-i). Glasses away from boundary layers have high V (~250-370
335 ppm), where concentrations primarily vary with phase assemblage and proportions and fO_2 (Table
336 1). They are relatively homogeneous in V (<20% and mostly <3% 2RSDs), where pairs of the
337 homogeneous glass and inclusion-free, near-rim mineral compositions yield V partitioning
338 coefficients for olivine-glass (~0.006-0.041), spinel-glass (~1.1-3.3), and clinopyroxene-glass

(~0.3-1.8) that compare to partition coefficients previously determined in other studies, and particularly to those of other low-temperature experiments (Fig. 2a-c; Table 1).

Approach to equilibrium for mineral-melt V partitioning

Pichavant et al. (2002) and Pichavant & Macdonald (2007) have inferred a close approach to total equilibrium for most of their STV301 experimental assemblages using established tests (i.e., experimental duration, textural evidence, homogeneous major- and minor-element phase compositions in individual charges as well as systematic compositional variation between charges, mineral-melt major-element partitioning coefficients in agreement with literature values, and low residuals in mass balance calculations), but highlighted partial disequilibrium for spinel and clinopyroxene. For our study, it is most important to identify partial equilibrium, i.e. equilibrium between the V compositions of selected mineral-glass compositional pairs.

(1) Homogenous textures and the lack of zoning in minerals and glasses of most charges is consistent with an approach towards equilibrium. Glass boundary layers around clinopyroxene (<5-10 μm wide), however, indicate partial disequilibrium. Clinopyroxene appears unzoned in BSE images, but crystals were too small to investigate trace-element zoning. The presence of core-rim zoning of spinel in all experiments and core-rim zoning of olivine in ≤1155 °C experiments also records partial disequilibrium. The cores of the zoned spinel crystals are inherited from the starting material (Fig. S1a), which have failed to dissolve completely during preparation of the starting glasses and during the experiments, as reported by Pichavant et al. (2002) and Pichavant & Macdonald (2007). The cores of the zoned olivine crystals (Fig. S2g-i), in contrast, have formed during the experiments, which are interpreted to reflect fast crystallization relative to diffusion and incomplete subsequent

362 equilibration. The presence of compositionally distinct cores of spinel and ±olivine had a
363 limited effect on phase compositions (e.g. some elements were preferentially retained in the
364 crystal cores), but it had no effect on our calculated partition coefficients and calculated
365 intensive parameters, as long as the unzoned near-rim mineral and main melt compositions
366 were in equilibrium.
367 (2) Unzoned olivine and unzoned spinel core and rim compositions and glass compositions of
368 individual charges show low V variation (<20% and mostly <3% 2RSDs) and calculated V
369 partition coefficients that are within the range of published values (Fig. 2a,b; Table 1),
370 which decrease with increasing fO_2 as expected (e.g., compared to data of Laubier et al.
371 2014; Shishkina et al. 2018; Wang et al. 2019), suggesting that they reflect equilibrium
372 partitioning. The calculated clinopyroxene-melt V partition coefficients also broadly
373 compare to published low-temperature data (Fig. 2c), falling between the partitioning
374 coefficients of Laubier et al. (2014) and Wang et al. (2019) and those of Toplis & Corgne
375 (2002) and Holycross & Cottrell 2022, and they decrease with increasing fO_2 as expected.
376 The presence of melt (now glass) boundary layers around clinopyroxene crystals
377 nevertheless indicates partial disequilibrium, but V compositions may not have been
378 significantly affected with partitioning coefficients close to unity (~0.3 and ~1.5) and thus
379 limited if any V enrichment or depletion in the melt boundary layers. Further below, we
380 therefore continue to assess if our clinopyroxene-melt V partitioning coefficients
381 approached equilibrium, evaluating them against inferred equilibrium partitioning data of
382 Laubier et al. (2014) and Wang et al. (2019).
383
384

385 ***Vanadium oxybarometry tests***

386 The focus of our study was on olivine-melt V oxybarometers, but we have also considered spinel-
387 melt and clinopyroxene-melt V oxybarometers, which may extend the range of applications. We
388 have tested overall performance of the calibrations and evaluated bias for calculated compared to
389 experimental fO_2 relative to experimental temperature, pressure, as well as mineral and melt
390 composition. Melt composition was considered through melt H_2O concentration and NBO/T
391 composition (i.e. the ratio of non-bridging oxygen to tetrahedral cations). Melt NBO/T is a first-
392 order approximation of melt polymerization, which was calculated as $NBO/T=(2X_O-4X_T)/X_T$ (cf.
393 Mysen et al. 1982), where X are the atomic proportions of oxygen (O) and tetrahedrally coordinated
394 cations ($T=Si^{4+}$, T^{i4+}, and P^{5+}, plus Al^{3+} and Fe^{3+} charge balanced by excess alkalis, with Fe^{3+}
395 calculated using the equation of Kress & Carmichael (1991)). In addition to anhydrous NBO/T
396 (commonly used, calculated from anhydrous glass compositions), we have calculated hydrous
397 NBO/T (calculated from hydrous glass compositions considering molecular H_2O concentrations
398 and formation of T-OH bonds, e.g. following Di Muro et al. 2006). Accounting for analytical
399 uncertainties in determining melt composition and especially melt H_2O concentration, we assign
400 uncertainties of 0.1 and 0.2, respectively, to the calculated anhydrous and hydrous NBO/T values.
401 We highlight that the structure of multi-component hydrous melts cannot yet be fully quantified
402 (e.g., Behrens 2020), and that the hydrous NBO/T values may not give a true image of melt
403 structure, but that they permit quantitative comparison of variably hydrous melts, accounting for
404 the fact that hydrous melt component are known to significantly affect melt polymerization.

405 To test the olivine-melt oxybarometers of Mallmann & O'Neill (2013), Shishkina et al.
406 (2018) (equation 4), and Wang et al. (2019) for primitive arc magmas, we have used the selected
407 hydrous to anhydrous experimental V partitioning data equilibrated at conditions (~ΔQFM-2.0 to

408 ΔQFM+4.0, ~1025 to 1350 °C, <10 wt% melt H_2O, 0 to 2000 MPa) that match those typical for
409 partial crystallization within the crust and upper mantle (Table S4). The starting materials of the
410 considered experimental studies were natural high-Mg basalts (our data and the data of Shishkina
411 et al. 2018), natural high-Mg basaltic andesite and mid-ocean ridge basalt (Laubier et al. 2014),
412 and synthetic high-Mg basalt mixed with peridotite (Wang et al. 2019). None of the test data were
413 part of the Mallmann & O'Neill (2013) calibration. However, the data of Laubier et al. (2014) and
414 Shishkina et al. (2018) were part of the Shishkina et al. (2018) calibration, and the data of Laubier
415 et al. (2014) and Wang et al. (2019) were part of the Wang et al. (2019) calibrations. Using some
416 of the oxybarometer calibration data enabled us to test the oxybarometers for the full range of
417 hydrous to anhydrous V partitioning data relevant for arc magmas, permitting direct comparison of
418 the different calibrations. The Shishkina et al. (2018) V oxybarometer is the simplest of the
419 evaluated calibrations in that it considers only the effect of fO_2 on olivine-melt partitioning, thus
420 showing most directly the possible effect of other intensive parameters on V partitioning and
421 oxybarometric estimates.

422 For the test data, the three olivine-melt oxybarometers calculate fO_2 values that are close to
423 the experimental fO_2 values considering uncertainties (Fig. 3a-c). The calculated and experimental
424 fO_2 values are (1) mostly within ±0.8 and 0.7 log units (2SDs) of each other for the Wang et al.
425 (2019) and Mallmann & O'Neill (2013) calibrations (Fig. 3a,b); and (2) mostly within ±0.4 log
426 units (2 SDs) of each other for the Shishkina et al. (2018) calibration, which was specifically
427 derived for hydrous, low-temperature equilibration (Fig. 3c). However, calculated compared to
428 experimental fO_2 values (expressed as ΔQFM (Calc-Exp) show systematic bias as a function of
429 various intensive parameters for all three calibrations (Figs 3d-l). Most of the data show concurring
430 trends, but the data of Wang et al. (2019) deviate from the correlation trends in some instances,

431 which we describe below. Test data outside the temperature calibration ranges (i.e. data equilibrated
432 at <1200 °C for MO2013, data equilibrated at <1150 °C for W2019, and data equilibrated at >1250
433 °C for S2018) or the two high-temperature (1350 °C) data, in contrast, do not systematically deviate
434 from correlation trends (Fig. 3). Using the Mallmann & O'Neill (2013) calibration, ΔQFM (Calc-
435 Exp) shows negative correlation with temperature (Fig. 3d; R^2=0.65) and no correlation with
436 pressure (Fig. S3a, R^2=0.06). ΔQFM (Calc-Exp) also shows no correlation with olivine forsterite
437 content (Fig. S3b), with anhydrous or hydrous NBO/T (Fig. 3g,j), or melt H_2O concentration (Fig.
438 S3c) for the entire test data. However, significant positive correlation is observed with hydrous
439 NBO/T (Fig. 3j) or melt H_2O concentration (Fig. S3c) without the Wang et al. (2019) data, which
440 show a subparallel, but offset trend. Using the Wang et al. (2019) calibration, ΔQFM (Calc-Exp)
441 shows negative correlation with temperature (Fig. 3e; R^2=0.35) and no correlation with pressure
442 (Fig. S3d; R^2=0.10). ΔQFM (Calc-Exp) and olivine forsterite content (Fig. S3e) or anhydrous
443 NBO/T (Fig. 3h; R^2=0.08) are uncorrelated, whereas ΔQFM (Calc-Exp) and hydrous NBO/T or
444 melt H_2O concentration are positively correlated (Fig. 3k and S3f). As for the Mallmann & O'Neill
445 (2013) calibration, the data of Wang et al. (2019) deviate from the hydrous NBO/T and melt H_2O
446 concentration correlation trends, but less significantly. Using the Shishkina et al. (2018) calibration,
447 ΔQFM (Calc-Exp) shows no correlation with temperature (Fig. 3f; R^2=0.03), but a weak positive
448 correlation with pressure (Fig. S3g; R^2=0.47). ΔQFM (Calc-Exp) and olivine forsterite content
449 (Fig. S3h) or anhydrous NBO/T (Fig. 3i) are uncorrelated, whereas ΔQFM (Calc-Exp) and hydrous
450 NBO/T (Fig. 3i; R^2=0.58) or melt H_2O concentration (Fig. S3i; R^2=0.49) are positively correlated.
451 As for the other two calibrations, the Wang et al. (2019) data slightly deviate from the hydrous
452 NBO/T and melt H_2O concentration correlation trends (Fig. 3l). That the Wang et al. (2019) data
453 tend to fall off the NBO/T and H_2O concentration correlation trends likely reflects (1) that their

melt H_2O concentrations are slightly overestimated (causing the limited offset visible in Fig. 3l), and (2) variable performance of the three calibrations for their relatively Na- and K-rich melt compositions (e.g. Figs 3j and k versus l).

The bias in ΔQFM (Calc-Exp) as a function of the various tested intensive parameters (typically ≤0.5-1.0 log units) may appear minor, but is important as it is on the order of the characteristic difference in fO_2 inferred for most arc (~QFM+0.5 to +3.5) compared to mid-ocean-ridge magmas (~QFM±0.5). The bias may moreover result in misinterpretation of the redox evolution of individual magma systems, such that false oxidation or reduction trends are calculated. Some of the observed correlations between fO_2 bias and various intensive parameters may be spurious (e.g. weak correlation with pressure may reflect co-correlation with hydrous NBO/T). However, temperature, pressure, and anhydrous as well as hydrous melt compositions are all known to affect mineral-melt element partitioning to some degree (Blundy & Wood 2003), and most of the parameters – i.e., temperature, olivine composition, and anhydrous NBO/T or anhydrous SiO_2-Al_2O_3-Na_2O-K_2O melt compositions – have been inferred to have a significant effect on olivine-melt V partitioning. An effect of melt H_2O concentration or hydrous NBO/T on olivine-melt V partitioning and thus calculated fO_2 values (Fig. 3j-l), which appears to be relevant for all three considered calibrations, in contrast, was ruled out by Shishkina et al. (2018) and Wang et al. (2019).

Like Shishkina et al. (2018) and Wang et al. (2019), we see only a weak correlation between ΔQFM (Calc-Exp) and melt H_2O concentration or hydrous NBO/T if we consider small datasets (e.g. only the data of Shishkina et al. (2018) or our new data). However, if we consider ΔQFM (Calc-Exp) and hydrous NBO/T or melt H_2O content for the to date largest possible high-quality dataset, as we have done above, or if we consider subsets of our data – i.e. compositions from experiments that were performed in the same IHPV run (at the same temperature and different melt

H_2O concentrations; e.g., our experiments 3-1 and 3-2, 4-1 and 4-2 etc.) – then we can see that ΔQFM (Calc-Exp) generally increases with increasing melt H_2O concentration and hydrous NBO/T (Fig. 3j-l, S3c,f,i; Table S4) Our conclusion is new for olivine-melt V partitioning, but in agreement with other studies who have experimentally shown that trace-element partitioning into silicate minerals is lower in equilibrium with hydrous than in equilibrium with anhydrous melt, which has been linked to the lower degree of polymerization of the hydrous relative to the anhydrous melts (Green et al. 2000; Gaetani et al. 2003; McDade et al. 2003).

Spinel-melt and clinopyroxene-melt V oxybarometers for arc magmas have recently been calibrated by Wang et al. (2019), which may provide an independent test relative to olivine oxybarometers and enlarge the application range, but all calibration data are from experiments equilibrated at >1150 °C, and they should thus be used with caution for arc magmas, as most clinopyroxene will have crystallized and most spinel will have equilibrated at lower temperature (e.g., Heath et al. 1998; Pichavant & Macdonald 2007). As for olivine above, we have used the selected hydrous to anhydrous test data, but our new data for clinopyroxene (n=2) and spinel (n=3) are too limited to conclusively assess oxybarometer accuracy or bias related to various intensive parameters. Our clinopyroxene-melt compositions and the selected subset of data from Wang et al. (2019) and data from Laubier et al. (2014), calculate redox state to mostly within ~±1.0 log units of the experimentally constrained conditions (Fig. S4a-c; Table S6). The estimates are thus moderately accurate for the test dataset, but there moreover appears to be bias, overestimating fO_2 for Al-rich clinopyroxene and underestimating fO_2 for Al-poor clinopyroxene compositions (Fig. S4b), indicating that the oxybarometer calibration overestimates the effect of clinopyroxene Al concentration, as was previously suspected by Holycross & Cottrell (2022). Our clinopyroxene-melt compositions are interpreted to have been in partial disequilibrium, but their V concentrations

500 seem to have approached equilibrium as much as the other test data, showing similar ΔQFM (Calc-
501 Exp). Our spinel-melt compositions and the selected subset of data from Wang et al. (2019)
502 calculate redox state to mostly within ~±0.8 log units of the experimentally constrained conditions
503 (Fig. S4d-f; Table S5). The estimates are thus reasonably accurate for the test dataset, but there also
504 appears to be bias, overestimating fO_2 for spinel crystallized at oxidizing conditions and
505 underestimating fO_2 for spinel crystallized at reducing conditions, likely relating to spinel
506 compositional variation in addition to Cr# (Fig. S4e; Table S4). For the small test datasets, which
507 are dominated by data employed in the calibrations, the ΔQFM (Calc-Exp) values show no clear
508 correlation with anhydrous or hydrous NBO/T (Fig. S4c,f; Tables S5 and S6). However, for
509 clinopyroxene, a subset of the data show positive correlation between ΔQFM (Calc-Exp) and
510 hydrous NBO/T, which we would suspect from our findings for olivine and from previous studies
511 (Green et al. 2000; Gaetani et al. 2003; McDade et al. 2003).

512

513 ***New olivine V oxybarometer calibrations***

514 Following, we now calibrate a new set of olivine-melt V oxybarometers with the aim to eliminate
515 the ΔQFM (Calc-Exp) bias of the evaluated olivine-melt V oxybarometers, using the same dataset
516 as for our tests above (Table S3). Step-wise linear regression for all intensive parameters considered
517 (i.e., temperature, pressure, olivine forsterite content, and anhydrous as well as hydrous NBO/T,
518 and melt H_2O concentration) confirmed a significant effect of hydrous NBO/T on V partitioning
519 and thus on ΔQFM (Calc-Exp). Effects from intensive parameters other than fO_2 and hydrous
520 NBO/T are not ruled out, but they are insignificant (with regression p-values>0.05) for the

considered calibration range, including temperature, or directly correlated with hydrous NBO/T (e.g. melt H_2O concentration).

In a first step, we use simple linear regression to define an oxybarometer as a function of olivine-melt V partitioning (Table 2):

fO_2 (ΔQFM) = –3.2848 –2.9893 x Log(D_V) (R^2=0.94, 2SD=0.4; Eqn 1).

In a second step, we use multiple linear regression to yield a more complex oxybarometer as a function of olivine-melt V partitioning and hydrous melt NBO/T (Table 2):

fO_2 (ΔQFM) = –2.8438 –3.1960 x Log(D_V) –0.8781 x h-NBO/T (R^2=0.97, 2SD=0.3; Eqn 2),

where fO_2 (ΔQFM) is the oxygen fugacity relative to the quartz-fayalite-magnetite buffer of O'Neill (1987) in log units, D_V is the olivine-melt V partitioning coefficient and h-NBO/T is the hydrous NBO/T value. The equation 1 oxybarometer shows a relatively high degree of correlation (R^2=0.94) and relatively low uncertainty (2SD=0.4 log units), but ΔQFM (Calc-Exp) bias as a function of hydrous NBO/T (Table S4). The oxybarometer closely compares to the oxybarometer of Shishkina et al. (2018), which can be used for estimating fO_2 in cases where melt composition including melt H_2O concentration is weakly constrained. More importantly, we suggest that the equation 1 oxybarometer is used for estimating Fe_2O_3/FeO concentrations needed to calculate melt NBO/T values (instead of assuming Fe_2O_3/FeO as is commonly done). The equation 2 calibration removes the ΔQFM (Calc-Exp) bias relative to hydrous NBO/T, but also relative to all other considered intensive parameters (e.g., removing spurious correlation for pressure or individual melt components), showing matching correlation trends for all individual test datasets. The equation

shows a high degree of correlation (R^2=0.97) and relatively low uncertainty (2SD=0.3 log units) (Fig. 4). Errors on estimates for unknowns can be calculated as:

σ (Eqn 1) = $(0.0279 + 0.0116 \times (\text{Log}(D_V))^2 + 8.9359 \times (\sigma(\text{Log}(D_V))^2)^{\wedge 0.5}$ and

σ (Eqn 2) = $(0.0159 + 0.0060 \times (\text{Log}(D_V))^2 + 10.2144 \times (\sigma(\text{Log}(D_V))^2 + 0.0127 \times (\text{h-NBO/T})^2 + 0.7711 \times \sigma(\text{h-NBO/T})^2)^{\wedge 0.5}$, accounting for regression errors as provided in Table 2 and requiring users to estimate σ for their Log(D_V) and hydrous melt NBO/T input values.

We stress (1) that the hydrous calibration dataset on which our olivine-melt oxybarometers are built remains limited, which should be supplemented by more high-quality experimental data in the future, especially for temperatures >1200 °C and hydrous NBO/T >1.2; and (2) that the oxybarometers should only be employed to phase compositions and intensive system parameters that closely match those of the calibration range, as provided in Table S3. We further suggest that our and other available mineral-melt V oxybarometers are best applied in concert and that the results are then interpreted in detail, as we do below in our case study of the natural St. Vincent high-Mg basalts.

The St. Vincent case study

Primitive high-Mg basalts erupted at Saint Vincent are primary and near-primary mantle-derived melts (Heath et al. 1998; Macdonald et al. 2000; Pichavant & Macdonald 2007; Melekhova et al. 2015). High-Mg basalt sample STV301 comprises olivine (~16 vol%), spinel (~2 vol%), and clinopyroxene (~9 vol%) phenocrysts with rare inherited xenocrystic or antecrystic cores, embedded in a crystallized, plagioclase-, clinopyroxene, olivine, and spinel-bearing matrix (Fig. S5). No glassy melt inclusions or interstitial glass are present, and potential crystallized melt

564 inclusions are rare (Fig. S5). Small potential crystallized melt inclusions (Fig. S5b) may be true
565 inclusions, whereas larger inclusions may be apparent, which were connected to
566 matrix/groundmass in 3D (Fig. S5a,d,e). The sample was previously petrologically studied by
567 Heath et al. (1998), Pichavant et al. (2002), and Pichavant & Macdonald (2007), who presented
568 major- and minor-element, but no trace-element compositional data.

569

570 ***Phenocryst textures and compositions***

571 Olivine phenocrysts of high-Mg basalt STV301 are subhedral to euhedral and up to ~2 mm in size.
572 They have locally spinel and potential crystallized melt inclusions and they rarely contain inherited
573 cores (~1 vol%), which are subround and devoid of inclusions (Fig. S5a,b, S6a-f). The olivine
574 phenocrysts show core-rim zoning with weakly zoned core plateau zones and significantly zoned
575 rims, or more complex zoning where inherited cores are present. The phenocryst cores have high
576 Fo (~84-90), low to intermediate CaO (~0.14-0.23 wt%) and MnO (~0.10-0.32 wt%), low V (~3.8-
577 6.3 ppm), intermediate to high Sc (~5.7-8.4 ppm), low Y (≤0.12 ppm), and intermediate to high Ni
578 (~1350-2600 ppm) (Fig. 5; Table S7). Their compositions match those of the experimental crystals,
579 except that the experimental crystals have overall higher CaO concentrations. The phenocryst rims
580 have lower Fo (~70-77) and Ni (~680-1060 ppm), yet higher MnO (~0.41-0.52 wt%), CaO (~0.26-
581 0.35 wt%), V (~8.0-16.1 ppm) and Y (≥0.15 ppm), and overall higher Sc (~7.1-8.6 ppm) than the
582 phenocryst cores and the experimental crystals (Fig. 5; Table S7). The inherited olivine cores have
583 compositions that are distinct from those of the phenocrysts and the experimental crystals with
584 moderately high Fo (~80-86), low CaO (≤0.07 wt%), low to intermediate MnO (0.08-0.32), and
585 low V (~2.1 ppm), Sc (~2.8), Y (~0.06 ppm), and Ni (~1000 ppm) (Fig. 5; Table S7).

586 Spinel in sample STV301 forms euhedral to skeletal phenocrysts up to ~200 μm in size and
587 small (<10 μm), or subhedral to euhedral inclusions in olivine and clinopyroxene that commonly
588 occur together with crystallized melt (Fig. S5b,d). The spinel phenocrysts and spinel inclusions
589 show gradational core-rim zoning in BSE imaging mode. The spinel inclusions have high to
590 intermediate Mg# (~45-58%), low to intermediate Fe^{3+}/R^{3+} (~7-13%) and low to high Fe^{3+}/Fe(tot)
591 (~20-36%) (Fig. 6a,b; Table S8). High-Mg# inclusions that were large enough for LA-ICP-MS
592 analysis have low V (~880 ppm), Sc (~5.7 ppm), and Y (≤0.04 ppm), and intermediate to high Ni
593 (~570-1150 ppm) (Fig. 6c-f; Table S8). The cores of spinel phenocrysts have overall lower Mg#
594 (~28-44%) and lower Fe^{3+}/R^{3+} and Fe^{3+}/Fe(tot) than the spinel inclusions at equivalent Mg# (Fig.
595 6a,b; Table S8). Compared to the analyzed spinel inclusions, the phenocryst cores have equivalent
596 to higher V (~870-1520 ppm), Sc (~4.7-11.6 ppm), and Y (~0.03-0.09 ppm), yet lower Ni (~390-
597 590 ppm) (Fig. 6c-f; Table S8). Both high-Mg# spinel inclusions and phenocryst cores have
598 compositions that match those of the low-Mg# experimental crystals. Spinel phenocryst rims have
599 low Mg# (~21-34%) and high Fe^{3+}/Fe(tot) (~42-49%), Fe^{3+}/R^{3+} (~26-49%), V (>2000 ppm) and
600 Sc (~12 ppm) relative to the phenocryst cores with concentrations that significantly also differ from
601 the experimental spinel compositions (Fig. 6; Table S8).

602 Clinopyroxene phenocrysts are subhedral to euhedral and typically <500 μm in maximum
603 dimension (Fig. S5c,d). Like olivine, the clinopyroxene phenocrysts locally contain inherited cores
604 (~2 vol%), which are anhedral, comprising coarsely crystallized melt inclusions (Fig. S5d). The
605 phenocrysts show sharp sector zoning with superimposed oscillatory zoning or more complex
606 zoning where inherited cores are present (Fig. S6j-e). The sector-zoned phenocrysts have
607 intermediate to high Mg# (~80-86%), low to high TiO_2 and Al_2O_3 (~0.5-1.4 and ~2.9-7.4 wt%) and
608 high CaO (~21.8-23.6 wt%) (Fig. 7a-c; Table S9). They also have low to high V (~210-400 ppm),

609 high Ni (~110-130 ppm) and Sc (~200-250 ppm), and low Y (~9-14 ppm) (Fig. 7d-f; Table S9).
610 Sector zoning is most prominent in Al_2O_3 and V (Fig. 7b, d-f). The phenocrysts have notably higher
611 Mg#, CaO and Sc, comparable V, Y, and Ni and lower Al_2O_3 than the experimental crystals,
612 showing no compositional match. The inherited clinopyroxene cores show complex patchy zoning
613 (Fig. S6j-l) with low Mg# (~73-76%), high TiO_2 (~0.9-1.3 wt%), low Al_2O_3 (~2.9-3.6 wt%) and
614 CaO (~20.2-21.1 wt%), and intermediate V (~360 ppm) concentrations (Fig. 7; Table S9). Their
615 Ni (~30-90 ppm) and Sc (~140-200 ppm) concentrations are low to intermediate, whereas their Y
616 concentration (~16-30 ppm) is intermediate to high. Their compositions are different from the
617 compositions of both the phenocrysts and the experimental crystals.

618

619 ***Melt compositions and mineral-melt partitioning coefficients***

620 High-Mg basalt STV301 comprises no glass inclusions or glassy matrix, and only a limited number
621 of large inclusions that may represent crystallized melt (Fig. S5), which could have been connected
622 to the matrix/groundmass in three dimensions, and we have therefore estimated melt compositions
623 (Fig. 8; Table 3). We highlight that it is common for primitive arc magmas such as STV301 that
624 melt inclusions are absent from phenocrysts or that the melt inclusions are in disequilibrium with
625 their phenocryst hosts (e.g., Bouvier et al. 2008, 2022). In our case study, we show that intensive
626 parameters using mineral-melt compositions can nevertheless be estimated for these rocks, if
627 equilibrium melt compositions are rigorously constrained. Following, we estimate melt
628 compositions for early-stage magma storage (estimates E1 to E3), where primitive phenocryst cores
629 formed (olivine+spinel), and late-stage magma storage (estimates E4 to E6), where evolved
630 phenocryst cores formed (olivine+spinel+clinopyroxene). Following Pichavant & Macdonald
631 (2007), we infer early- to late-stage magma storage at depth at ~400 MPa, at volatile saturated

conditions, and in equilibrium with a hydrous melt with ~5 wt% H_2O. Strongly zoned phenocryst rims and matrix crystals – which have equivalent size and compositions (e.g. <Fo80 olivine) – are inferred to have crystallized or re-equilibrated during magma ascent to the surface and subsequent to eruption, for which equilibrium melt compositions could not be estimated.

During early-stage storage crystallization, olivine, spinel and melt ±fluid were the stable phases of the STV301 magma (Pichavant and Macdonald 2007). Following Heath et al. (1998) and Pichavant & Macdonald (2007), we suggest that the most primitive olivine cores (~Fo89, ~4.0-5.6 ppm V, ~5.7-7.4 ppm Sc, ~0.06-0.08 ppm Y, and ~1780-2590 ppm Ni; Fig. 5; Table S7) crystallized at this stage. Spinel inclusions and phenocrysts were present, but have at least partly equilibrated at lower temperature (in Mg-Fe but possibly also in V), with calculated olivine-spinel equilibration temperatures of ≤1130 °C (cf. Heath et al. 1998). Following common practice (e.g., Putirka 2008), we estimate that the early-stage storage melt composition has approached bulk-rock composition (E1), but that it was slightly more evolved owing to minor crystallization of olivine and spinel and the presence of inherited crystal cores in our sample STV301, in agreement with Pichavant & Macdonald (2007), who experimentally showed that the primary STV301 melt was slightly less primitive (lower in MgO) than the STV301 whole rock. Our best estimate for early-stage storage melt composition are the experimental STV301 glass composition 7-2 in equilibrium with ~3 vol% olivine and ~1 wt% spinel (estimate E2) and a melt composition calculated considering crystallization of olivine and spinel and the presence of inherited crystal cores (combined ~6 wt% olivine, ~1 wt% spinel, and ~2 wt% clinopyroxene) (estimate E3) (Tables 3 and S10). The estimated E2 and E3 melt compositions with ~284-291 ppm V, ~42-44 ppm Sc, ~14.1-14.8 ppm Y, and ~180-230 ppm Ni at ~9.8-10.2 wt% MgO (Table 3) closely match, except for their Ni concentrations (Fig. 8). Their compositions fall onto primitive Saint Vincent whole-

655 rock compositional trends (Fig. 9; Table 3) and they moreover match the MgO concentrations of
656 primitive olivine-hosted melt inclusions of other high-Mg basalts from Saint Vincent (reported by
657 Bouvier et al. 2008, 2010), but they have overall lower V and Y contents. The difference in
658 estimated STV301 melt and measured melt inclusion V and Y compositions likely reflects variable
659 magma/melt compositions and fO_2 for the studied STV301 magma from the Pre-somma unit and
660 for younger high-Mg magmas (likely from the Yellow Tuff formation) sampled by Bouvier et al.
661 (2008, 2010). Alternatively, the difference in V and Y compositions could record formation of V-
662 and Y-rich melt boundary layers around olivine that were enclosed as melt inclusions, in line with
663 olivine-melt inclusion isotopic disequilibrium detected for a large proportion of the inclusions
664 (Bouvier et al. 2022). In combination, our best estimates for the early-stage storage melt
665 composition (estimates E2 and E3) and the primitive olivine phenocryst core compositions (Table
666 3) calculate Fe(tot)-Mg partitioning coefficients of ~0.23 to 0.24, which are in the range of
667 equilibrium values for moderately oxidizing crystallization conditions (cf. Blundy et al. 2020), thus
668 suggesting that the estimated melt compositions E2 and E3 and primitive olivine phenocryst cores
669 indeed represent or approach equilibrium pairs. The olivine and melt (E2 and E3) compositions
670 further calculate a limited range of V partition coefficients of ~0.014-0.020 and Sc/Y and Ni
671 partition coefficients of ~24-46 and ~7.8-15 (Table 3), which translate into a small variation in
672 calculated fO_2 (≤0.15 log units difference) and a limited to moderate variation in calculated
673 temperatures (<30 °C for Sc/Y versus <75 °C for Ni) (Table 4).

674 During late-stage storage conditions (prior to magma ascent towards eruption), olivine,
675 clinopyroxene, spinel, and melt ±fluid were the stable phases of the STV301 magma (Pichavant
676 and Macdonald 2007). Following again the interpretation of Heath et al. (1998) and Pichavant &
677 Macdonald (2007), we suggest that the evolved olivine core (~Fo84-86, ~4.2-5.1 ppm V, ~5.8-8.0

678 ppm Sc, ~0.04-0.10 ppm Y, and ~1350-2000 ppm Ni), Mg-rich spinel phenocryst core (Mg#~40-
679 50%, ~870-980 ppm V), and clinopyroxene phenocryst core (Mg#>80%, ~210-400 ppm V, ~200-
680 250 ppm Sc) compositions crystallized or equilibrated at this stage (Tables S5-S7). Following
681 common practice (e.g. Putirka 2008), we have attempted to calculate the late-stage storage melt
682 composition, subtracting phenocryst and inherited core compositions from the STV301 bulk rock
683 composition (estimate E4) (Tables 3 and S11). The estimated E4 melt composition falls along
684 primitive Saint Vincent whole-rock compositional trends (Fig. 8), but is too evolved to have been
685 in equilibrium with ~Fo84-86 olivine, calculating an Fe(tot)-Mg partitioning coefficient of ~0.16
686 (Table 3), reflecting the difficulty to accurately constrain the phenocryst and inherited crystal core
687 cargos and their average compositions. Moderately evolved experimental STV301 glass
688 compositions (averages of experimental glasses 3-1 and 3-2) and the matrix/groundmass
689 composition of the natural STV301 sample (estimates E5 and E6) are taken as alternative
690 constraints (Table 3). The average experimental glass composition was taken to account for partial
691 crystallization (~7.5 wt% olivine, ~0.5 wt% spinel, and ~7.0 wt% clinopyroxene). The composition
692 of the matrix/groundmass was analyzed with a broad, 100 μm beam away from phenocrysts,
693 averaging a total of 20 analyses. Compared to our estimates of the early-stage storage melt, the E5
694 and E6 melt estimates for the late-stage storage melt remain uncertain given the difficulty to
695 precisely estimate the proportion of phenocryst cores that have been present at this stage (especially
696 for complexly zoned clinopyroxene, which may have crystallized during late-stage storage or
697 magma ascent). However, both estimated E5 and E6 compositions fall along Saint Vincent whole-
698 rock compositional trends (Fig. 8) and they moreover match the MgO and characteristic Y
699 concentrations of evolved olivine-hosted melt inclusions of other high-Mg basalts from Saint
700 Vincent (Fig. 8) . The calculated Fe(tot)-Mg partitioning coefficients for olivine and estimated melt
701 compositions E5 and E6 are ~0.23-0.25 (Table 3), which are in the range of equilibrium values for

moderately oxidizing crystallization conditions (cf. Blundy et al. 2020), moreover suggesting that the E5 and E6 melt and evolved olivine core compositions indeed represent or approach equilibrium pairs (Table 3). The compositions further calculate olivine-melt V, Sc/Y, and Ni partition coefficients of ~0.013-0.018, ~31-59 and ~15-26, and spinel-melt V partitioning coefficients of ~2.8-3.4 (Table 3). The clinopyroxene phenocrysts show complex sector and oscillatory zoning, and they were therefore not used for estimating equilibrium partitioning coefficients or crystallization conditions below. As for the early-stage storage conditions, our best estimates for the late-stage storage melt compositions (E5 and E6) translate into a small variation in calculated fO_2 (≤0.15 log units difference) and a limited to moderate variation in calculated temperatures (<70 °C for Sc/Y versus <30 °C for Ni) (Table 4).

Temperature and fO_2 of the primitive St. Vincent magma during early-stage storage

Average temperatures calculated for early-stage storage olivine and inferred equilibrium-melt (E2 and E3) compositions are ~1210±30 °C using the Sc/Y olivine-melt thermometer of Mallmann & O'Neill (2013) and ~1240±60 °C using the Ni olivine-melt thermometer of Pu et al. (2017) (Table 4). The calculated Ni temperature appears high, but the calculated Sc/Y temperature closely approaches the experimentally constrained near-liquidus temperature of ~1200 °C of Pichavant & Macdonald (2007), which in combination suggest that the three tested olivine-melt V oxybarometers and our new calibration are all applicable to the inferred mineral-melt equilibrium pairs. To estimate the early-stage storage fO_2, we then use the minimum and maximum V concentrations of Fo-rich olivine, the various estimated melt compositions, and a temperature estimate of ~1200 °C (Tables 3 and 4). We assume a melt H_2O concentration of ~5 wt% as experimentally constrained by Pichavant & Macdonald (2007) and as has been detected in primitive

olivine-hosted melt inclusions from other St. Vincent high-Mg basalts (Bouvier et al. 2008), which is consistent with the observation that olivine phenocryst core CaO compositions match or most closely approach those crystallized in H_2O-rich experiments (~≥5 wt% H_2O) (Fig. 5a) (cf. Gavrilenko et al. 2016). For these parameters, the various olivine-melt oxybarometers calculate fO_2 values of ~QFM+1.4 to QFM+2.4 and on average ~QFM+1.8 to QFM+2.1 ±0.5-0.9 log units (Fig. 9a; Table 4). The range of estimated melt compositions (E2 and E3) has a limited effect on the inferred fO_2 (Δ ≤0.15 log units) and Sc/Y temperature (Δ ~30 °C) (Table 4), as melt V, Sc, and Y contents show limited variation after crystallization of minor olivine and traces of spinel and can therefore be fairly well constrained (Fig. 8). The inferred Ni temperatures, in contrast, are more variable (Δ <65 °C), reflecting the difficulty to tightly constrain olivine-melt Ni equilibrium pairs. The range of detected trace-element concentrations in Fo-rich olivine (ΔV ~1.6 ppm, ΔSc ~1.7 ppm, ΔY ~0.02 ppm; Table S7) are significantly larger than the analytical errors (≤0.24 ppm V, ≤0.37 ppm Sc, ≤0.006 ppm; Table S7), thus likely recording true variation in crystallization conditions, which could reflect fO_2 variation by up to 0.3 log units, temperature variation by up to 60 °C, or variation in other intensive parameters between magma parcels and their phenocryst cargo.

The reason that all applied V oxybarometers calculate closely concurring fO_2 values is consistent with equilibration at relatively high temperature (~1200 °C), but we posit that all previous calibrations and our equation 1 oxybarometer nevertheless tend to systematically overestimate fO_2 for the hydrous magma T(cf. Fig. 3). The estimated average fO_2 values of ~QFM+1.8 to QFM+2.1±0.5-0.9 and our best estimate of ~QFM+1.8±0.5 (calculated using our equation 2 calibration) are overall lower than but within the uncertainty of the previous fO_2 estimate of ~QFM+2.1 to +2.6 of Pichavant & Macdonald (2007) (Fig. 9a). We suggest that our new fO_2

748 estimate is more accurate for early-stage crystallization conditions than the previous estimate,
749 which was based on the composition of small, high-Mg#, high $Fe^{3+}/Fe(tot)$ spinel inclusions, which
750 have partially equilibrated in Mg-Fe with their olivine hosts, consistent with olivine-spinel
751 equilibration temperatures of ≤1130 °C (Heath et al. 1998). Our redox estimate of ~QFM+1.8±0.5
752 for the early-storage, near-liquidus, mantle-derived STV301 melt is within the range of values
753 characteristic for primitive Lesser Antilles magmas, which vary between ~QFM+0.5 to QFM+4.3
754 and are mostly ~QFM+1.0 to QFM+3.0 (Heath et al. 1998; Pichavant & Macdonald 2007; Stamper
755 et al. 2014). Our estimate is also within the range of values considered characteristic for arc settings
756 constrained using various mineral-melt oxybarometers, phase-equilibrium experiments and recent
757 whole-rock geochemical modelling (~QFM+0.5 to QFM+3.5, e.g., Gaillard et al. 2015; Bucholz &
758 Kelemen 2019). The inferred early-stage storage, near-liquidus fO_2 is, however, significantly
759 higher than fO_2 values (~QFM) inferred for primitive mantle-derived arc magmas using the bulk-
760 rock V/Sc or Ga/Sc models of Lee et al. (2005) or Mallmann & O'Neill (2009).

761

762 ***Temperature and fO_2 of the primitive St. Vincent magma during late-stage storage***

763 Average temperatures calculated for the late-stage storage olivine-melt (E4 and E5) compositional
764 pairs are ~1080±30 °C using the Sc/Y olivine-melt thermometer of Mallmann &O'Neill (2013)
765 and ~1130±60 °C using the Ni olivine-melt thermometer of Pu et al. (2017) (Table 4). The
766 calculated Sc/Y temperature agrees with the experimentally constrained late-stage storage
767 temperatures of ~1050-1100 °C of Pichavant & Macdonald (2007), whereas the Ni thermometer
768 appears to overestimate temperature as for the early-stage storage conditions. To estimate the late-
769 stage storage fO_2, we therefore take a temperature of ~1075 °C, which suggests that the mineral-
770 melt pairs equilibrated outside the calibration range of the Mallmann & O'Neill (2013) and Wang

et al. (2019) V oxybarometers. To estimate the late-stage storage fO_2, we nevertheless employ all tested and our new olivine-melt V oxybarometers and the spinel-melt V oxybarometer of Wang et al. (2019) to assess and discuss the different results. We use the minimum and maximum V concentrations of the evolved olivine phenocryst core compositions (~Fo84-86), Mg-rich spinel phenocryst core compositions (~Mg#40-60) and estimated (E4 and E5) melt compositions (Table 3). As for the early-stage storage conditions, we assume a melt H_2O concentration of ~5 wt% (cf. Pichavant & Macdonald 2007; Bouvier et al. 2008), given that melt inclusions from St. Vincent and Lesser Antilles magmas in general record volatile (H_2O-CO_2) saturation at ≥5 wt% (cf. Balcone-Boissard et al. (2023)) and given that the STV301 olivine/melt Ca contents show no significant increase with decreasing olivine Fo content (Fig. 5a), which would be expected in the case of significant variation of melt H_2O concentration (cf. Gavrilenko et al. 2016). For these parameters, the various olivine-melt and the spinel-melt oxybarometers calculate fO_2 values of ~QFM+1.9 to QFM+3.1and on average ~QFM+2.1 to QFM+2.9 ±0.5-0.9 log units, which are much more variable (differing by ~0.8 log units) than the fO_2 values calculated for the early-stage storage condition (differing by ~0.3 log units) (Fig. 9a versus 9b; Table 4). Our equation 1 and 2 olivine-melt V oxybarometers calculate the lowest fO_2 values of ~QFM+2.1±0.6 on average, whereas the Wang et al. (2019) spinel-melt and the Mallmann & O'Neill (2013) and Wang et al. (2019) olivine-melt oxybarometers calculate higher fO_2 values of ~QFM+2.6±0.5, ~QFM+2.7±0.5 and ~QFM+2.9±0.5 on average (Fig. 9b, Table 4). The range of estimated late-stage storage melt (E4 and E5) compositions has a slightly higher, but still limited effect on the calculated fO_2 (Δ <0.2 log units) compared to the early-stage storage melt. The reason for this is that the crystallization of several weight percent of clinopyroxene in addition to olivine significantly fractionates melt V and that equilibrium mineral-melt compositions become more difficult to constrain. The range of trace-

794 element concentrations in Mg#-rich spinel and in Fo-rich olivine phenocryst cores (ΔV ~100 ppm
795 for spinel; ΔV ~0.9 ppm, ΔSc ~1.7 ppm, ΔY ~0.06 ppm for olivine; Table S4) are significantly
796 larger than the analytical errors (≤30 ppm V for spinel; ≤0.18 ppm V, ≤0.29 ppm Sc, and ≤0.01
797 ppm Y for olivine) and for olivine on the same order as for the primitive phenocryst cores,
798 suggesting that intensive parameters varied to the same degree (e.g. fO_2 by ~0.3 log units or
799 temperature by ~60 °C), which could indicate that smaller magma parcels and their phenocryst
800 cargo were blended just prior to eruption.

801 We take an average fO_2 of ~QFM+2.1±0.6, calculated using our olivine-melt V
802 oxybarometers, as the best estimate for the late-stage storage fO_2 (Fig. 9b; Table 4). That our and
803 the Shishkina et al. (2018) oxybarometers calculate closely comparable fO_2 for low-temperature
804 equilibration (~QFM+2.1 and ~QFM+2.2) and relatively less oxidized fO_2 values than the
805 Mallmann & O'Neill (2013) and Wang et al. (2019) calibrations was expected (cf. Fig. 3), which
806 highlights that it is critically important to have tight temperature constraints for the crystallization
807 of the redox-sensitive assemblage, and that the Mallmann & O'Neill (2013) and Wang et al. (2019)
808 oxybarometers should not be applied outside their calibration range at below ~1200-1150 °C. That
809 our oxybarometers and the Shishkina (2018) (equation 4) calibration calculate closely matching
810 values reflects the relatively polymerized character of the estimated equilibration melt (h-NBO of
811 ~0.84-0.97; Table 3) with intermediate melt H_2O concentration (~5 wt%) yet otherwise evolved
812 composition (cf. Figs 3l, S4f). Our best estimate of ~QFM+2.1±0.6 falls between the previous
813 estimates of Pichavant & Macdonald (2007) (~QFM+2.1 to QFM+2.6 based on their phase
814 equilibrium experiments and spinel compositions) and Heath et al. (1998) (~QFM+1.5 to QFM+1.8
815 using the Ballhaus et al. (1991) olivine-spinel oxybarometer) (Fig. 10b), which is slightly higher
816 than our fO_2 estimate for early-stage storage (~QFM+1.8) by ~0.3 log units, which may indicate a

817 limited fO_2 increase during intermittent crustal storage. If the results from the Mallmann & O'Neill
818 (2013) or Wang et al. (2019) oxybarometers would have been considered, then more significant
819 oxidation by ~0.8 log units may have been erroneously inferred. Results from our equation 1 or the
820 Shishkina et al. (2018) oxybarometers, which do not account for melt compositional variation other
821 than in V, in contrast would have suggested no essential oxidation (i.e. by ≤0.1 log units).

822

823 **Limited oxidation during intermittent crustal storage of the STV301 magma**

824 Our best fO_2 estimates for early-stage to late-stage storage suggest limited oxidation by ~0.3 log
825 units during intermittent crustal magma storage, but such limited redox variation is within the
826 uncertainty of our method (±0.3 log units) and smaller than the estimated individual uncertainties
827 (±0.5-0.6 log units) (Table 4). Considering the extremes of individual uncertainties, V
828 oxybarometry alone cannot rule out limited reduction (by ~0.8 log units, i.e. from QFM+1.8+0.5
829 to QFM+2.1-0.6) or more significant oxidation (by ~1.4 log units, i.e. from QFM+1.8-0.5 to
830 QFM+2.1+0.6) for the STV301 magma during intermittent crustal storage. However, limited
831 evidence for contamination (i.e. presence of minor amounts of inherited crystal cores) and lack of
832 evidence for degassing during magma storage in combination with crystallization of moderate
833 amounts of olivine (~7.5-10.5 wt%), clinopyroxene (~6.0-8.0 wt%), and spinel (~0.5-2.5 wt%), are
834 in agreement with limited oxidation. Redox variation of primitive magmas largely owing to
835 fractional crystallization of moderate amounts of olivine, clinopyroxene, and spinel (<25 wt%) is
836 typically inferred to be ≤0.5 log units as estimated for natural samples (Cottrell & Kelley 2011;
837 Kelley & Cottrell 2012), but may be higher, e.g. ~0.8 log units as shown in fractionation
838 experiments (Ulmer et al. 2018). For single samples like the studied STV301 basalt, such limited
839 redox variation cannot be reliably resolved by V olivine-melt or other mineral-melt oxybarometry.

However, V mineral-melt oxybarometry for a large number of samples from a single magma system, ideally with well-constrained melt compositions and large degrees of fractionation, have the capacity to establish if primitive arc magmas typically experience oxidation by ~0.5, ~1.0, or more log units. To track autoxidation for large degrees of fractional crystallization (>>25 wt%), which has been suggested to be as high as ≥4 log units based on fractionation experiments (Ulmer et al. 2018), V oxybarometers will have to be rigorously calibrated for lower-temperature equilibria for clinopyroxene-melt, spinel-melt, and/or amphibole-melt.

CONCLUSIONS

Olivine-melt and spinel-melt V oxybarometry have the potential to further improve our understanding of the redox state and redox evolution of Earth's primitive magmas. For robust constraints and to resolve limited fO_2 variation, it is however essential that the effects of temperature and anhydrous to hydrous melt polymerization on fO_2 estimates are considered. If they are neglected, olivine-melt and spinel-melt compositions may variably over- or under-estimated fO_2 by commonly up to ±1 log unit. This has important implications for constraining fO_2 for magmas generated at different geodynamic settings and for constraining redox evolution of magmas during partial crystallization. For primitive, high-Mg basaltic STV301 magma erupted at St. Vincent, Lesser Antilles, new olivine-melt V oxybarometry indicates oxidizing near-liquidus conditions (~QFM+1.8±0.5), consistent with the notion that arc magmas are primarily oxidized. During intermittent crustal storage, limited oxidation (by ~0.3 log units) appears to have occurred, in agreement with redox variation largely controlled by <25 wt% fractionation of olivine-clinopyroxene-spinel, but such limited oxidation cannot be reliably resolved by V or other mineral-melt oxybarometry for individual samples (with uncertainties of ≥±0.3-0.9 log units), requiring

863 characterization of a large number of samples to establish representative averages or other
864 characterization methods.

865

866 **ACKNOWLEDGEMENTS**

867 This work is part of the project "Tracking the differentiation of redox-sensitive elements in fluid-
868 rich to fluid-poor magmas" of Erdmann et al. supported by LabEx VOLTAIRE (ANR-10-LABX-
869 100-01). The analytical facilities at ISTO that were used are also supported by LabEx VOLTAIRE
870 (ANR-10-LABX-100-01) and by EquipEx PLANEX (ANR-11-EQPX-0036). Patricia Benoist and
871 Ida Di Carlo are thanked for their assistance and guidance in SEM imaging and electron microprobe
872 analyses. Fai Tcha and Henrique da Mota of IRAMAT are thanked for their support of ISTO's LA-
873 ICP-MS laboratory. Emmanuel Le Trong kindly helped with regression-related questions. The
874 Laboratoire Magmas et Volcans is thanked for hosting SE for a six-month stay in 2023. We
875 sincerely thank M. Holycross, an anonymous reviewer, and O. Müntener for their insightful and
876 constructive comments on an earlier version of this manuscript.

877

878 **REFERENCES**

879 Allen RW, Collier JS, Stewart AG, Henstock T, Goes S, Rietbrock A, Wilkinson JJ (2019) The
880 role of arc migration in the development of the Lesser Antilles: A new tectonic model for
881 the Cenozoic evolution of the eastern Caribbean. Geology 47: 891-895

882 Balcone-Boissard H, Boudon G, d'Augustin T, Erdmann S, Deloule E, Vicente J (2023)
883 Architecture of the Lesser Antilles arc illustrated by melt inclusions. J Petrol, egad020,
884 https://doi.org/10.1093/petrology/egad020

885 Behrens H (2020) Water speciation in oxide glasses and melts. Chem Geol 558: 119850

886 Blundy J, Wood B (2003) Partitioning of trace elements between crystals and melts. Earth and
887 Planetary Science Letters 210: 383-397

888 Blundy J, Melekhova E, Ziberna L, Humphreys MCS, Cerantola V, Brooker RA, McCammon CA,
889 Pichavant M, Ulmer P (2020) Effect of redox on Fe–Mg–Mn exchange between olivine and
890 melt and an oxybarometer for basalts. . Contrib Mineral Petrol 175: 103Bouvier A-S,
891 Métrich N, Deloule E (2008) Slab-derived fluids in magma sources of St.Vincent (Lesser
892 Antilles Arc): Volatile and light element imprints. J Petrol 49, 1427-1448

893 Bouvier A-S, Deloule E, Métrich N (2010) Fluid inputs to magma sources of St.Vincent and
894 Grenada (Lesser Antilles): New insights from trace elements in olivine-hosted melt
895 inclusions. J Petrol 51, 1597-1615

896 Bouvier A-S, Rose-Koga EF, Nichols ARL, Le Lay C (2022) Melt inclusion formation during
897 olivine recrystallization: Evidence from stable isotopes. Earth Plan Sci Lett 592: 117638

898 Brounce MN, Kelley KA, Cottrell E (2014) Variations in Fe^{3+}/Fe of Mariana arc basalts and mantle
899 wedge fO_2. J Petrol 55: 2513-2536

900 Brounce M, Stolper E, Eiler J (2022) The mantle source of basalts from Reunion Island is not more
901 oxidized than the MORB source mantle. Contrib Mineral Petrol 177:7

902 Bucholz CE, Kelemen PB (2019) Oxygen fugacity at the base of the Talkeetna arc, Alaska. Contrib
903 Mineral Petrol 174:79

904 Canil D (1997) Vanadium partitioning and the oxidation state of Archaean komatite magmas.
905 Nature 389: 842-845

906 Canil D (2002) Vanadium in peridotites, mantle redox and tectonic environments: Archean to
907 present. Earth Plan Sci Lett 195: 75-90

908 Canil D, Fedortchouk Y (2001) Olivine–liquid partitioning of vanadium and other trace elements,
909 with applications to modern and ancient picrites. Can Mineral 39:319-330

910 Carmichael ISE (1991) The redox states of basic and silicic magmas: a reflection of their source
911 regions? Contrib Mineral Petrol 106: 129-141

912 Cooper GF, Davidson JP, Blundy JD (2016) Plutonic xenoliths from Martinique, Lesser Antilles:
913 evidence for open system processes and reactive melt flow in island arc crust. Contrib
914 Mineral Petrol 171:87

915 Cottrrell E, Kelley KA (2011) The oxidation state of Fe in MORB glasses and the oxygen fugacity
916 of the upper mantle. Earth Plan Sci Lett 305: 270-282.

917 Davis FA, Humayun M, Hirschmann MM, Cooper RS (2013) Experimentally determined
918 mineral/melt partitioning of first-row transition elements (FRTE) during partial melting of
919 peridotite at 3 GPa. Geochim Cosmochim Acta 104: 232-260

920 Devine JD, Gardner JE, Brack HP, Layne GD, Rutherford MJ (1995) Comparison of
921 microanalytical methods for estimating H2O contents of silicic volcanic glasses. Am
922 Mineral 80: 319-328

923 Di Muro A, Villemant B, Montagnac G, Scaillet B, Reynard B (2006) Quantification of water
924 content and speciation in natural silicic glasses (phonolite, dacite, rhyolite) by confocal
925 microRaman spectrometry. Geochim Cosmochim Acta 70: 2868-2884

926 Evain M, Galvé A, Charvis Ph, Laigle M, Kopp H, Bécelc A, Weinzierl W, Hirn A, Flueh ER,
927 Gallart J, the Lesser Antilles Thales scientific party (2013) Structure of the Lesser Antilles
928 subduction forearc and backstop from 3D seismic refraction tomography. Tectonophysics
929 603: 55-67

930 Gaetani GA, Kent AJR, Grove TL, Hutcheon ID, Stolper EM (2003) Mineral/melt partitioning of
931 trace elements during hydrous peridotite partial melting. Contrib Mineral Petrol 145: 391–
932 405

933 Gaillard F, Scaillet B, Pichavant M, Iacono-Marziano G. (2015) The redox geodynamics linking
934 basalts and their mantle sources through space and time. Chem Geol 418: 217-233

935 Gavrilenko M, Herzberg C, Vidito C, Carr MJ, Tenner T, Ozerov A (2016) A calcium-in-olivine
936 geohygrometer and its application to subduction zone magmatism. J Petrol 57: 1811-1832.

937 Green TH, Blundy JD, Adam J, Yaxley GM (2000) SIMS determination of trace element partition
938 coefficients between garnet, clinopyroxene and hydrous basaltic liquids at 2–7.5 GPa and
939 1080–1200 °C. Lithos 53: 165-187

940 Grocke SB, Cottrell E, de Silva S, Kelley KA (2016) The role of crustal and eruptive processes
941 versus source variations in controlling the oxidation state of iron in Central Andean magmas.
942 Earth Plan Sci Lett 440: 92-104

943 Grove TL, Till CB, Krawczynski, MJ (2012). The role of H_2O in subduction zone magmatism.
944 Annu. Rev. Earth Planet. Sci. 2012. 40:413–39

945 Heath E, Macdonald R, Belkin H, Hawkesworth C, Sigurdsson H (1998) Magmagenesis at
946 Soufrière Volcano, St. Vincent, Lesser Antilles Arc. J Petrol 39: 1721-1764

947 Holycross M, Cottrell E (2022) Experimental quantification of vanadium partitioning between
948 eclogitic minerals (garnet, clinopyroxene, rutile) and silicate melt as a function of
949 temperature and oxygen fugacity. Contrib Mineral Petrol 177:21

950 Hughes EC, Buse B, Kearns SL, Blundy JD, Kilgour G, Mader HM (2019) Low analytical totals
951 in EPMA of hydrous silicate glass due to sub-surface charging: obtaining accurate volatiles
952 by difference. Chem Geol 505:48–56

953 Karner JM, Papike JJ, Sutton SR, Shearer CK, Burger P, McKay G, Le L (2008) Valence state
954 partitioning of V between pyroxene-melt: Effects of pyroxene and melt composition, and
955 direct determination of V valence states by XANES. Application to Martian basalt QUE
956 94201 composition. Meteorit Planet Sci 8: 1275-1285

957 Kelley KA, Cottrell E (2012) The influence of magmatic differentiation on the oxidation state of
958 Fe in a basaltic arc magma. Earth Plan Sci Lett 329-330: 109-121.

959 Laubier M, Grove TL, Langmuir CH (2014) Trace element mineral/melt partitioning for basaltic
960 and basaltic andesitic melts: An experimental and laser ICP-MS study with application to
961 the oxidation state of mantle source regions. Earth Plan Sci Lett 392: 265-278.

962 Lee C-TA, Leeman WP, Canil D, Li ZXA (2005) Similar V/Sc systematics in MORB and arc
963 basalts: Implications for the oxygen fugacities of their mantle source regions. J Petrol 46:
964 2313-2336

965 Macdonald R, Hawkesworth CJ, Heath E (2000) The Lesser Antilles volcanic chain: a study in arc
966 magmatism. Earth Sci Rev 49: 1-76

967 Mallmann G, O'Neill HSC (2009) The crystal/melt partitioning of V during mantle melting as a
968 function of oxygen fugacity compared with some other elements (Al, P, Ca, Sc, Ti, Cr, Fe,
969 Ga, Y, Zr and Nb). J Petrol 50: 1765-1794

970 Mallmann G, O'Neill HSC (2013) Calibration of an empirical thermometer and oxybarometer
971 based on the partitioning of Sc, Y and V between olivine and silicate melt. J Petrol 54: 933-
972 949

973 McDade P, Blundy JD, Wood BJ (2003) Trace element partitioning between mantle wedge
974 peridotire and hydrous MgO-rich melt. Am Mineral 88: 1825-1831

975 Melekhova E, Blundy J, Robertson R, Humphreys MC (2015) Experimental evidence for polybaric
976 differentiation of primitive arc basalt beneath St. Vincent, Lesser Antilles. J Petrol 56: 161-
977 192

978 Moussallam Y, Oppenheimer C, Scaillet B, Gaillard F, Kyle P, Peters N, Hartley M, Berlo K,
979 Donovan A (2014) Tracking the changing oxidation state of Erebus magmas, from mantle
980 to surface, driven by magma ascent and degassing. Earth Planet Sci Lett 393: 200-209

981 Moussallam Y, Edmonds M, Scaillet B, Peters N, Gennaro E, Sides I, Oppenheimer C (2016) The
982 impact of degassing on the oxidation state of basaltic magmas: a case study of Kīlauea
983 volcano. Earth Planet Sci Lett 450: 317-325

984 Mysen BO, Virgo D, Seifert FA (1982) The structure of silicate melts: implications for chemical
985 and physical properties of natural magma. Rev Geophys Space Phys 20: 353-383

986 O'Neill HSC (1987) Quartz-fayalite-iron and quartz-fayalite-magnetite equilibria and the free-
987 energy of formation of fayalite (Fe_2SiO_4) and magnetite (Fe_3O_4). Am Mineral 72: 67-75

988 Papike JJ, Burger PV, Bell AS, Le L, Shearer CK, Sutton SR, Jones J, Newville M (2013)
989 Developing vanadium valence state oxybarometers (spinel-melt, olivine-melt, spinel-
990 olivine) and V/(Cr plus Al) partitioning (spinel-melt) for martian olivine-phyric basalts. Am
991 Mineral 98: 2193-2196

992 Paton C, Hellstrom J, Paul B, Woodhead J, Hergt J (2011) Iolite: Freeware for the visualisation and
993 processing of mass spectrometric data. J Anal At Spectrom 26: 2508-2518

994 Petrus JA, Chew DM, Leybourne MI, Kamber BS (2017) A new approach to laser-ablation
995 inductively-coupled-plasma mass-spectrometry (LA-ICP-MS) using the flexible map
996 interrogation tool “Monocle”. Chem Geol 463: 76-93

997 Pichavant M, Mysen BO, Macdonald R (2002) Source and H_2O content of high-MgO magmas in
998 island arc settings: An experimental study of a primitive calc-alkaline basalt from St.
999 Vincent, Lesser Antilles arc. Geochim Cosmochim Acta 66: 2193-2209

1000 Pichavant M, Macdonald R (2007) Crystallization of primitive basaltic magmas at crustal pressures
1001 and genesis of the calc-alkaline igneous suite: experimental evidence from St. Vincent,
1002 Lesser Antilles arc. Contrib Mineral Petrol 154: 535-558

1003 Prytulak J, Sossi PA, Halliday AN, Plank T, Savage PS, Woodhead JD (2017) Stable vanadium
1004 isotopes as a redox proxy in magmatic systems? Geochem Perspect Lett 3: 75-84

1005 Pu X, Lange R, Moore G (2017) A comparison of olivine-melt thermometers based on D_{Mg} and
1006 D_{Ni}: The effects of melt composition, temperature, and pressure with applications to MORBs
1007 and hydrous arc basalts. Am Mineral 102: 750-765

1008 Putirka KD (2008) Thermometers and barometers for volcanic systems. Rev Mineral Geochem 69:
1009 61–120

1010 Righter K, Sutton SR, Newville M, Lei L, Schwandt CS, Uchida H., Lavina B, Downs RT (2006)
1011 An experimental study of the oxidation state of vanadium in spinel and basaltic melt with
1012 implications for the origin of planetary basalt. Am Mineral 91: 1643-1656

1013 Righter K, Herd CDK, Boujibar A (2020) Redox processes in early Earth accretion and in terrestrial
1014 bodies. Elements 16: 161-166

1015 Shishkina T, Portnyagin M, Botcharnikov RE, Almeev RR, Simonyan AV, Garbe-Schönberg D,
1016 Schuth S, Oeser M, Holtz F (2018) Experimental calibration and implications of olivine-
1017 melt vanadium oxybarometry for hydrous basaltic arc magmas. Am Mineral 103: 369-383.

1018 Stamper CC, Melekhova E, Blundy JD, Arculus RJ, Humphreys MCS, Brooker RA (2014)
1019 Oxidised phase relations of a primitive basalt from Grenada, Lesser Antilles. Contrib
1020 Mineral Petrol 167:954

1021 Tang M, Erdman M, Eldridge G, Lee C-TA (2018) The redox “filter” beneath magmatic orogens
1022 and the formation of continental crust. Sci Adv 4: eaar4444

1023 Tang M, Lee C-TA, Costin G, Höfer HE (2019) Recycling reduced iron at the base of magmatic
1024 orogens. Earth Plan Sci Lett 528:115827

1025 Tollan PME, Bindeman I, Blundy JD (2012) Cumulate xenoliths from St. Vincent, Lesser Antilles
1026 Island Arc: a window into upper crustal differentiation of mantle-derived basalts. Contrib
1027 Mineral Petrol 163: 189-208

1028 Toplis MJ, Corgne A (2002) An experimental study of element partitioning between magnetite,
1029 clinopyroxene and iron-bearing silicate liquids with particular emphasis on vanadium.
1030 Contrib Mineral Petrol 144: 22–37

1031 Ulmer P, Kaegi R, Müntener O (2018) Experimentally derived intermediate to silica-rich arc
1032 magmas by fractional and equilibrium crystallization at 10 GPa: an evaluation of phase
1033 relationships, compositions, liquid lines of descent and oxygen fugacity. J Petrol 59: 11–58

1034 Van Achterbergh E, Ryan CG, Griffin WL (2000). GLITTER on-line interactive data reduction for
1035 the LA-ICPMS microprobe. Sydney, Australia: Macquarie Research Ltd.

1036 Vanucci R, Tiepolo M, Defant MJ, Kepezhinskas P (2007) The metasomatic record in the shallow
1037 peridotite mantle beneath Grenada (Lesser Antilles arc). Lithos 99:25-44

1038 Wang J, Xiong X, Takahashi E, Zhang L, Li L, Liu X (2019) Oxidation state of arc mantle revealed
1039 by partitioning of V, Sc and Ti between mantle minerals and basaltic melts. J Geophys Res
1040 Solid Earth 124: 4617-4638

1041

1042

FIGURE CAPTIONS

Figure 1: Conditions of experiments for which V partitioning was quantified for olivine-melt, spinel-melt, or clinopyroxene-melt in this and in previous studies. Dataset used in this study (summarized in Tables S4 to S6) and datasets used by Shishkina et al. (2018) (S2018) and Wang et al. (2019) (W2019) for their V oxybarometers for arc magmas for comparison.

Figure 2: Mineral-melt partition coefficients determined for the STV301 experimental charges (Table 1) compared to published experimental data. Redox-sensitive V partition coefficients for (a) olivine-melt, (b) spinel-melt, and (c) clinopyroxene-melt. Ol=olivine, Cpx=clinopyroxene, Spl=spinel, L=melt. Literature data are from Canil (1997) (C1997), Toplis & Corgne (2002) (TC2002), Righter et al. (2006) (R2006), Karner et al. (2008) (K2008), Mallmann & O'Neill (2009, 2013) (MO2009, MO2013), Davis et al. (2013) (D2013), Papike et al. (2013) (P2013), Laubier et al. (2014) (L2014), Shishkina et al. (2018) (S2018), Wang et al. (2019) (W2019), and Holycross & Cottrell (2022) (HC2022). Errors for our partition coefficients are indicated as 2 RSDs, which are commonly smaller than the symbol size. Estimated errors on fO_2 and temperature are ±0.5 and ±1.0 log units and ±5 and ±25 °C for our internally heated pressure vessel and piston cylinder experiments, respectively.

Figure 3: Calculated ΔQFM versus experimentally-constrained ΔQFM (first row, a-c,), experimental temperature (T) versus ΔQFM (Calc-Exp) (second row, d-f,), calculated anhydrous NBO/T versus ΔQFM (Calc-Exp) (third row, g-i), and calculated hydrous NBO/T versus (ΔQFM (Calc-Exp) (fourth row, j-l) for the three tested oxybarometers. Calculated data shown were determined using the oxybarometers of Mallmann & O'Neill (2013) (first column (a,d,g,j), Eqn M2013), Wang et al. (2019) (second column (b,e,h,k,), Eqn W2019), and Shishkina et al. (2018) (third column (c,f,i,l,), Eqn S2018). Test data are from Laubier et al. (2014) (n=22), Shishkina et

al. (2018) (n=12), Wang et al. (2019) (n=11), and our study (n=9) Indicated uncertainties are estimated experimental and calibration uncertainties. All input and calculated data are provided in Table S4.

Figure 4: Calculated versus experimental fO_2 for our equation 2 olivine-melt V oxybarometer. (a) Calculated fO_2 values show limited deviation from experimental values. (b-f) Calculated compared to experimental fO_2 (ΔQFM (Calc-Exp)) values show no systematic bias in relation to crystallization temperature, pressure, olivine forsterite (Fo) content, or anhydrous or hydrous melt NBO/T (R^2 is always <0.05). The two V partitioning data from Wang et al. (2019) for olivine-melt equilibrated at 1350 °C do not significantly deviate from all other (≤1200 °C) data. Temperature thus does not appear to significantly affect V partitioning for the investigated temperature range between ~1025 and 1350 °C, but a limited effect (as predicted by Mallmann & O'Neill (2013) or Wang et al. (2019)) needs to be further investigated. Indicated uncertainties are – as for Fig. 3 – estimated experimental and calibration uncertainties. All data are reported in Table S4.

Figure 5: Olivine compositions, where forsterite (Fo) content was calculated as Fo=Mg/(Mg+Fe)*100. Olivine phenocryst cores have compositions that largely match the compositions of the experimental STV301 olivine, whereas inherited cores and phenocryst rim compositions differ. The STV301 olivine compositions are from this study (round symbols) and the study of Heath et al. (1998) (square symbols). Our STV301 data and their uncertainties are reported in Tables 1 and S7. Shown for comparison are olivine compositions of low-Mg basalts from St. Vincent (LMB) (Heath et al. 1998), Grenada basaltic to andesitic lavas (Stamper et al. 2014), St. Vincent and Grenada cumulates (Tollan et al. 2012; Stamper et al. 2014), and peridotite xenoliths including primary and secondary olivine (Vanucci et al. 2007).

Figure 6: Spinel compositions, where spinel Mg# was calculated as $Mg/(Mg+Fe^{2+})*100$, Fe^{3+} was calculated through charge balance, and R^{3+} was calculated as the sum of Al, Cr, and Fe^{3+}. The Mg#-rich spinel phenocryst cores and inclusions are close in composition to the experimental STV301 spinel, but the inclusions have overall higher Mg#, $Fe^{3+}/Fe(tot)$, and Fe^{3+}/R^{3+}. The STV301 spinel compositions are from this study (round symbols) and the study of Heath et al. (1998) (square symbols). Our STV301 data and their uncertainties are reported in Tables 1 and S8. Shown for comparison are spinel compositions of low-Mg basalts from St. Vincent (LMB) (Heath et al. 1998), Grenada basaltic to andesitic lavas (Stamper et al. 2014), St. Vincent and Grenada cumulates (Tollan et al. 2012; Stamper et al. 2014), and peridotite xenoliths (Vanucci et al. 2007).

Figure 7: Clinopyroxene compositions, where Mg# was calculated as $Mg/(Mg+Fe)*100$. Sector-zoned clinopyroxene phenocrysts and inherited cores differ from each other in composition and they also differ from the composition of the experimental STV301 clinopyroxene. The STV301 clinopyroxene compositions are from this study (round symbols) and the study of Heath et al. (1998) (square symbols). Our STV301 data and their uncertainties are reported in Tables 1 and S9. Shown for comparison are clinopyroxene compositions of low-Mg basalts from St. Vincent (LMB) (Heath et al. 1998), Grenada basaltic to andesitic lavas (Stamper et al. 2014), and St. Vincent and Grenada cumulates (Tollan et al. 2012; Stamper et al. 2014) and peridotite xenoliths including primary and secondary clinopyroxene (Vanucci et al. 2007).

Figure 8: Estimated early-stage storage (E1 to E3) and late-stage storage (E4 to E6) melt compositions for the STV301 magma (see Table 3 for full compositions and uncertainties). Our best estimates are compositions E2 and E3 for early-stage storage and E5 and E6 for late-stage storage conditions. Shown for comparison are the compositions of olivine-hosted melt inclusion compositions for other high-Mg basalts from St. Vincent (Bouvier et al. 2010, possibly from a

1111 sample of the Yellow Tuff formation), and St. Vincent whole-rock compositions (extracted from
1112 the GEOROC database). (b and e) are close-ups of (a and d) as indicated.

1113 **Figure 9:** Calculated average fO_2 values for the St. Vincent STV301 magma at early-stage and
1114 late-stage storage conditions for the different melt proxies and in comparison to previous estimates
1115 (see Table 4 for all calculated values). (a) All calculated fO_2 values for early-stage, near-liquidus
1116 condition are relatively close to each other, varying between ~QFM+1.8 and ~QFM+2.1 with our
1117 best estimate at ~QFM+1.8. (b) Calculated fO_2 values for late-stage storage condition vary over a
1118 large range, between ~QFM+2.1 and ~QFM+2.9. Indicated uncertainties (±0.5 log units in (a) and
1119 ±0.6 log units in (b)) are for our best estimates based on equation 2. All other uncertainties (±0.5-
1120 0.9) are given in Table 4. Previous estimates are from Heath et al. (1998) (H1998) and Pichavant
1121 & Macdonald (2007) (PM2007), which are based on olivine±spinel composition. Calibrations of
1122 Mallmann & O'Neill (2013) (MO2013), Shishkina et al. (2018) (S2018), Wang et al. (2019)
1123 (W2019), and our new calibrations (Eqn 1 and 2).

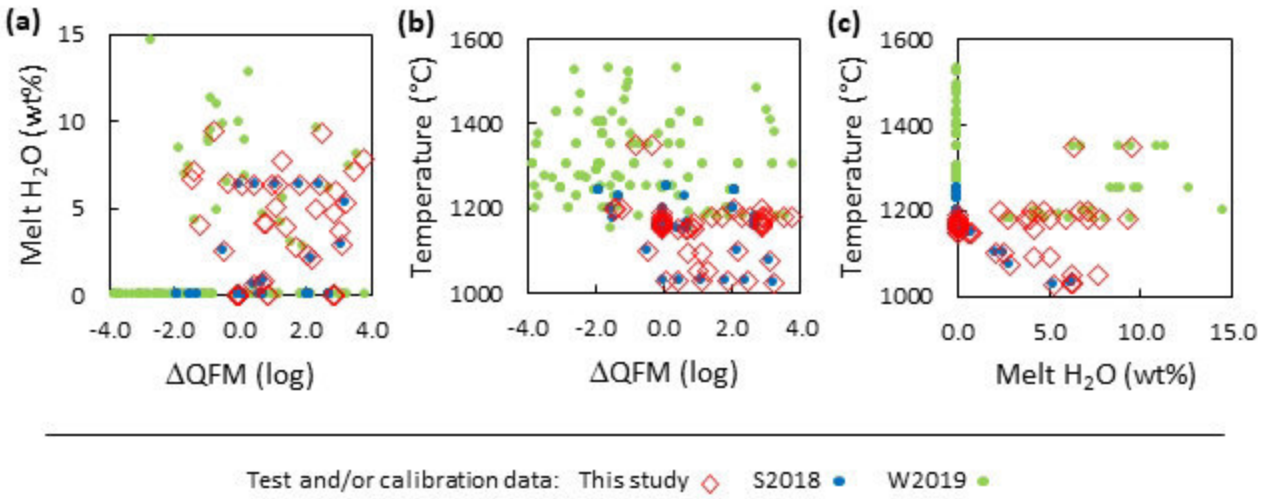

Figure 1 – Erdmann et al.

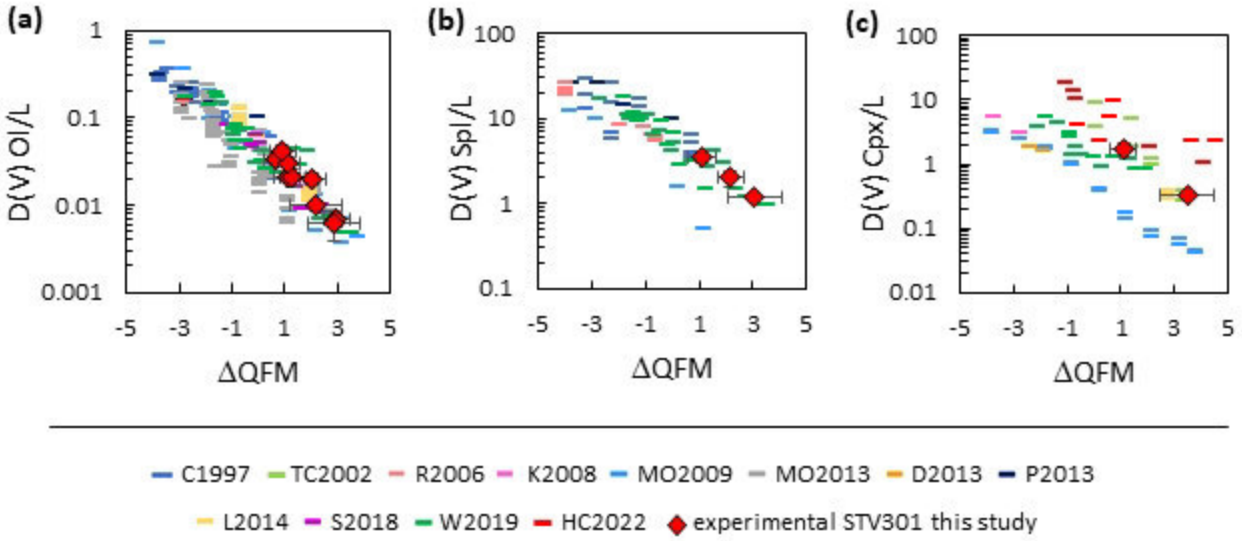

Figure 2 – Erdmann et al.

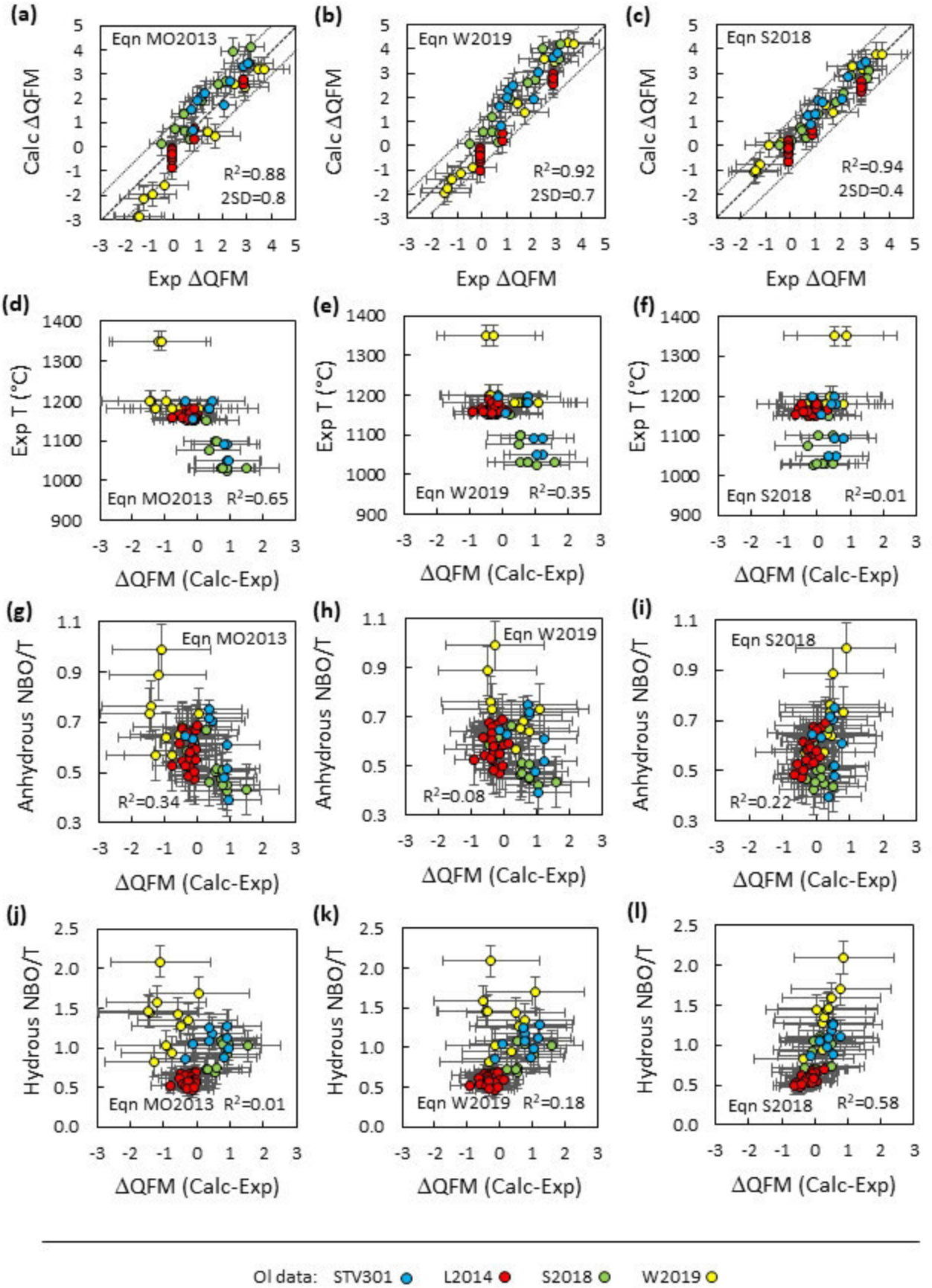

Figure 3 – Erdmann et al.

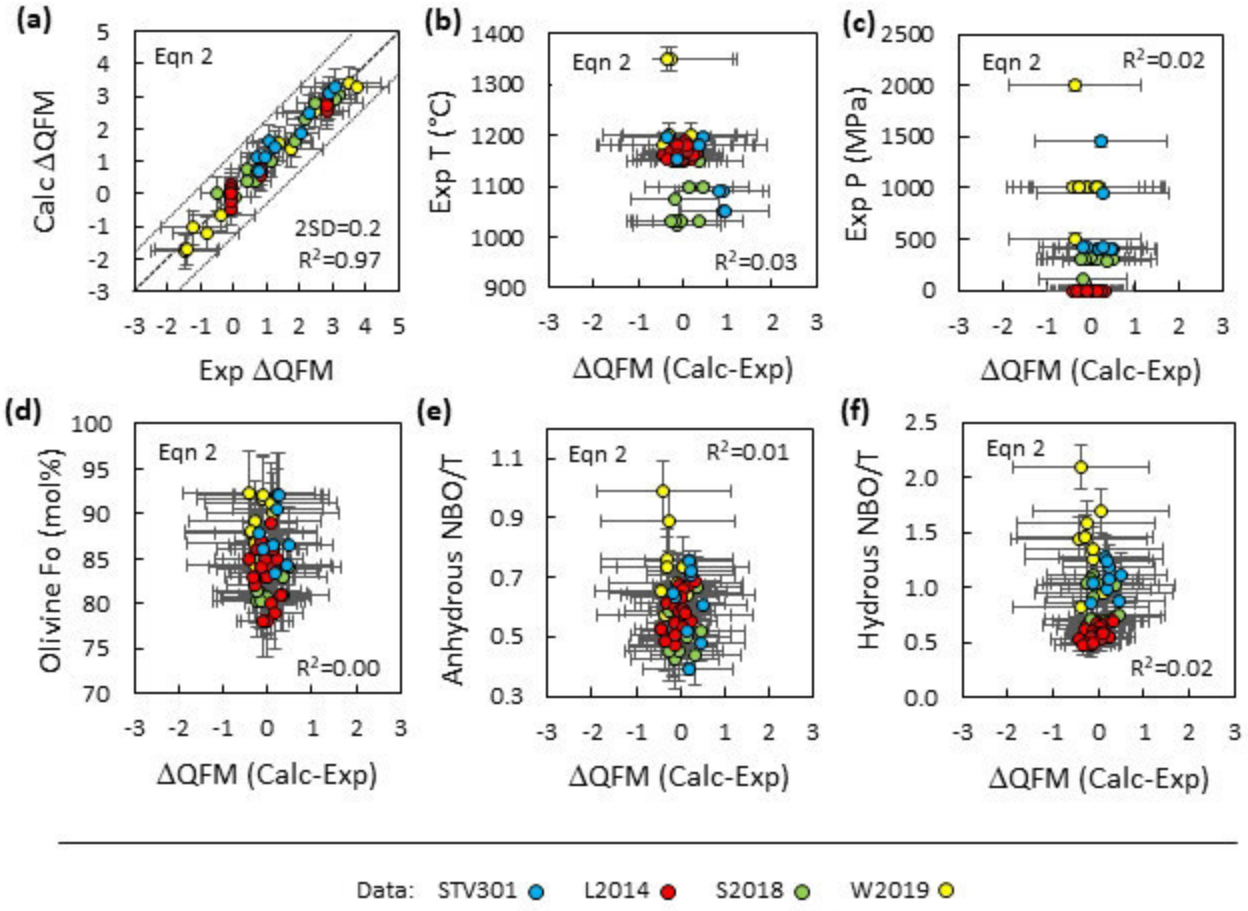

Figure 4 – Erdmann et al.

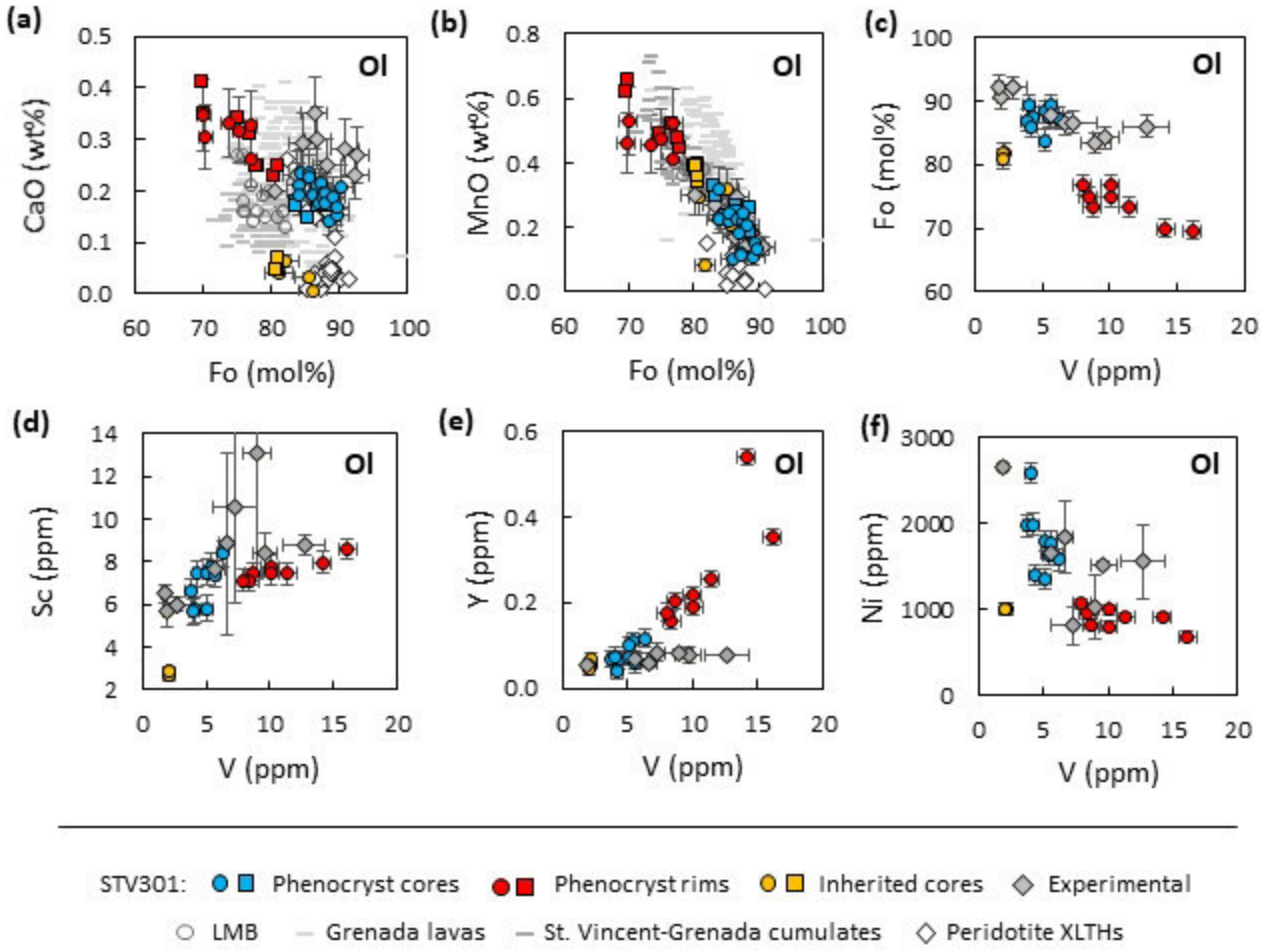

Figure 5 – Erdmann et al.

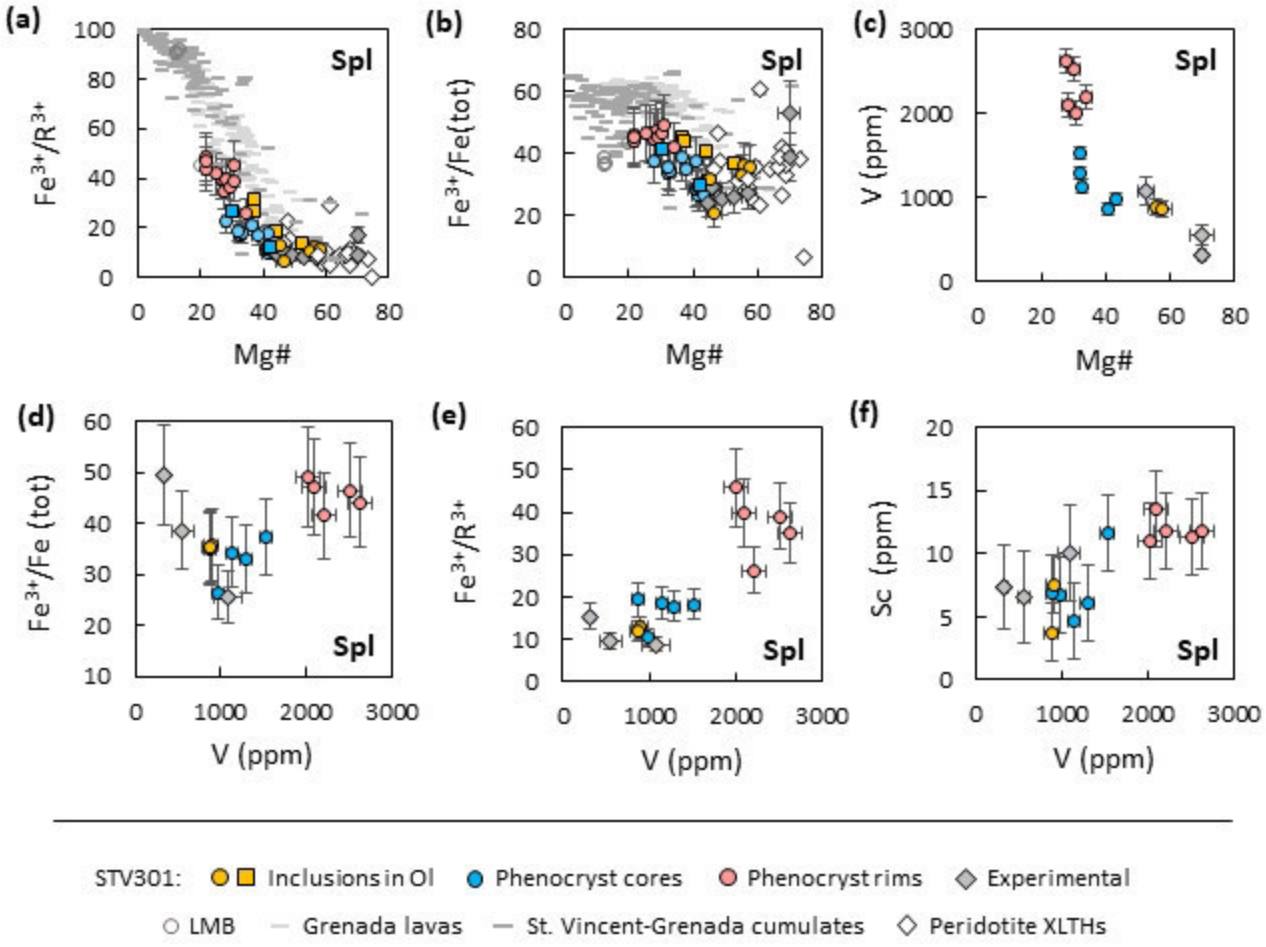

Figure 6 – Erdmann et al.

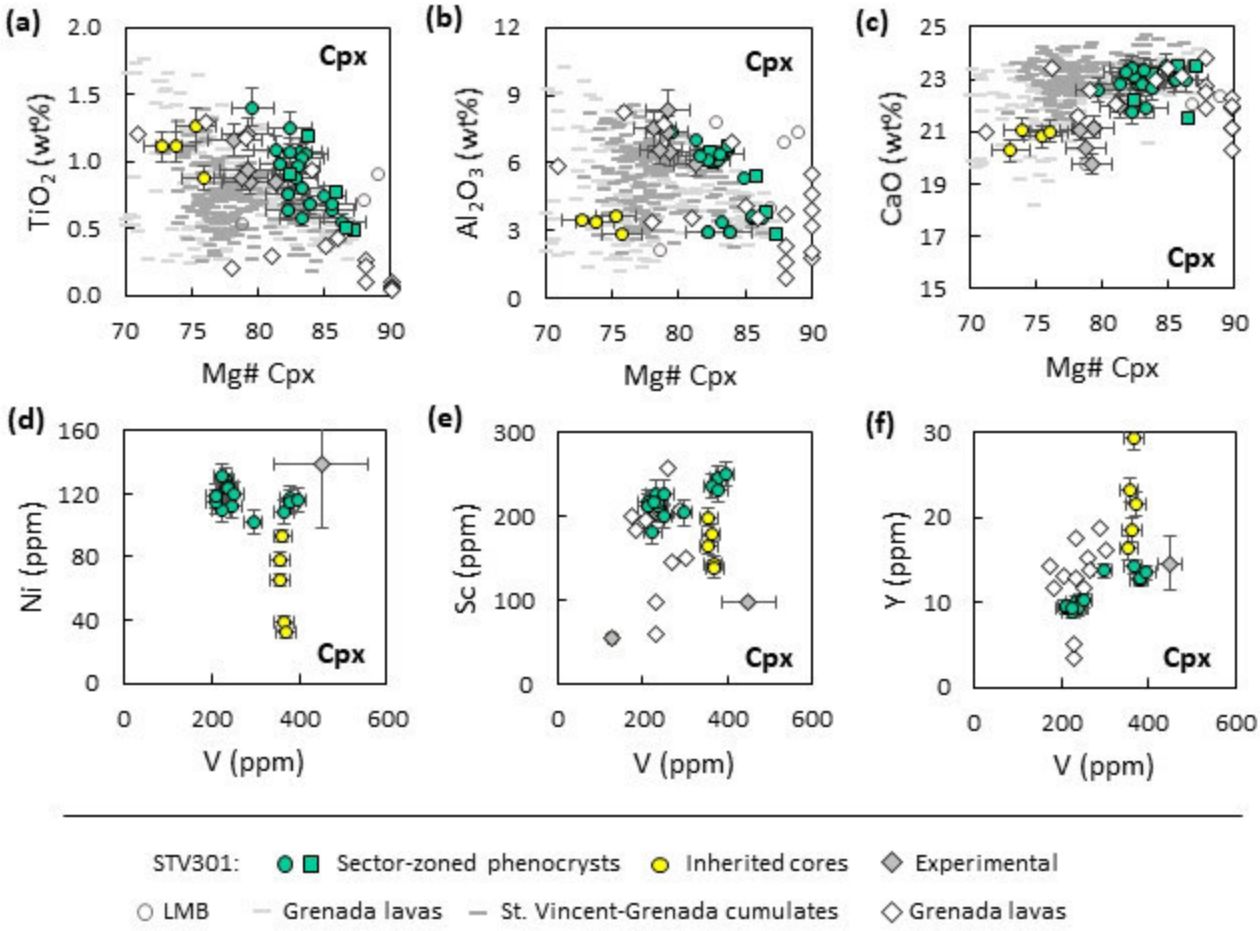

Figure 7 – Erdmann et al.

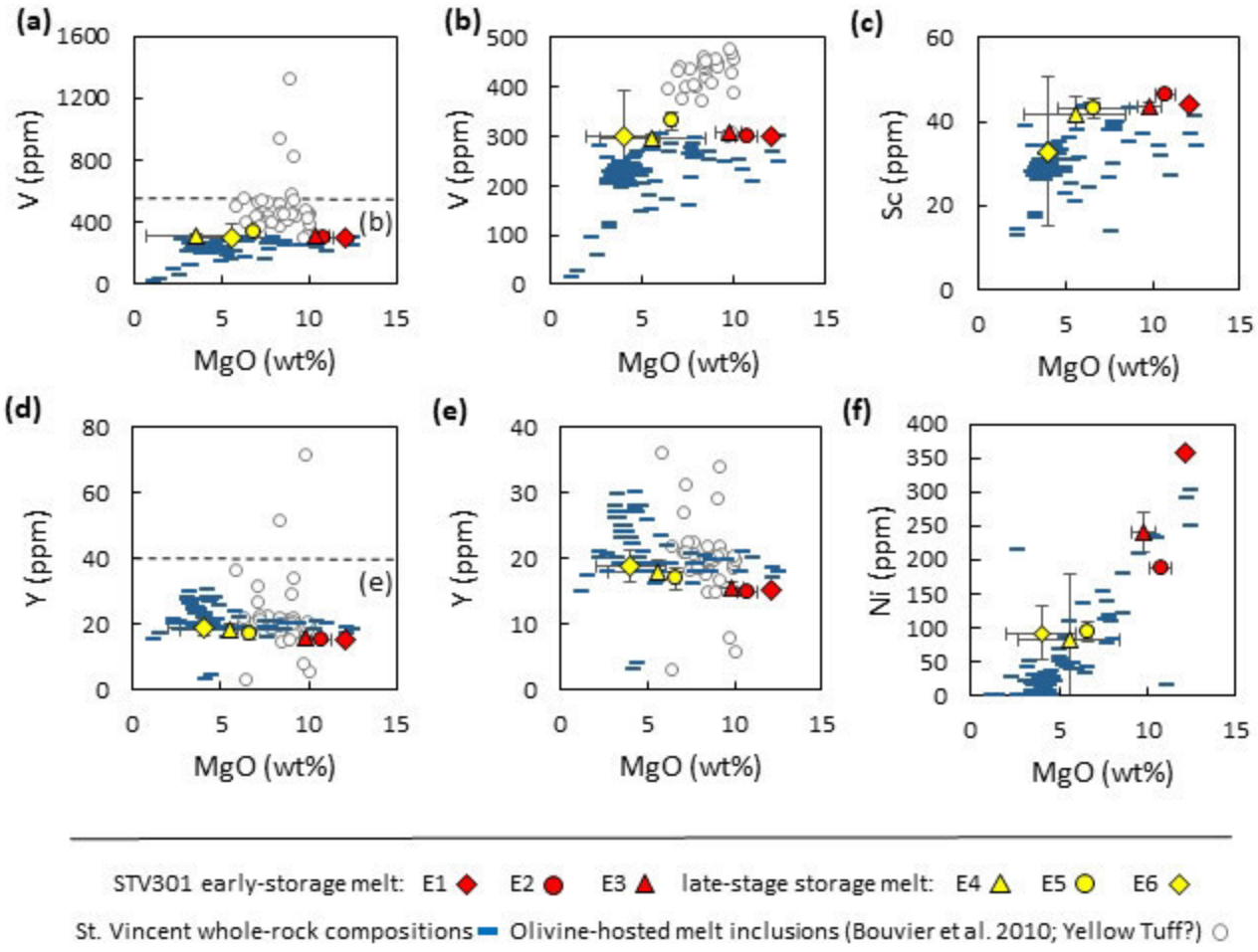

Figure 8 – Erdmann et al.

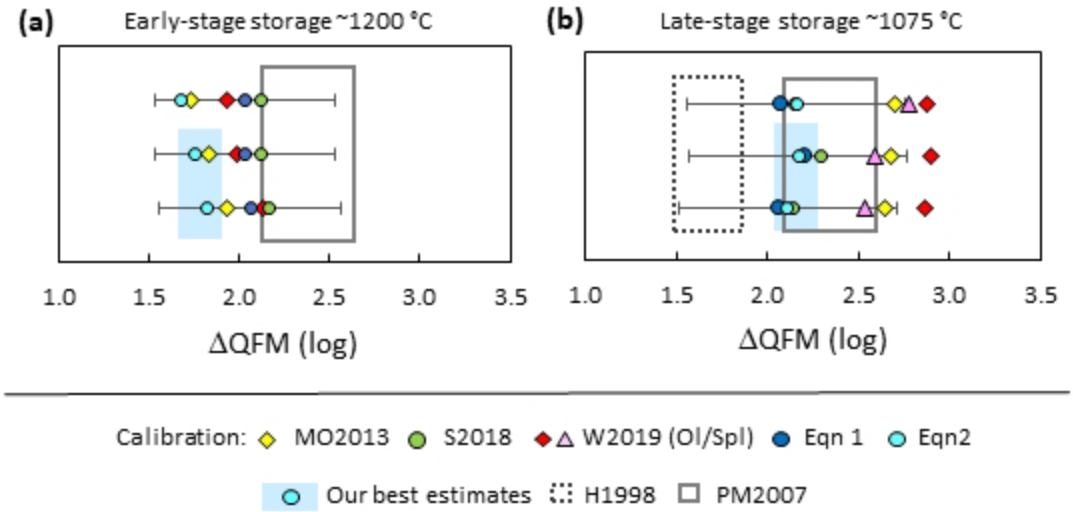

Figure 9 – Erdmann et al.

Table 1: Experimental details, V compositions, and partitioning coefficients of minerals and glasses

Charge	Ref. Exp.	Temp. Press.	ΔQFM (log)	Melt H_2O (wt%)	Assemblage	Phase (n)	V ppm(2RSD%)
4-1	PM2007 IHPV	1050 °C 400 MPa	1.3	7.7	Gl-Ol-Spl-Cpx-Q	Gl(10) Ol(5) D-Ol/L	353(2.8) 7.31(23.6) 0.021(25.0)
4-2	PM2007 IHPV	1050 °C 400 MPa	1.0	6.3	Gl-Ol-Spl-Cpx-Q	Gl(10) Ol(5) D-Ol/L	297(8.0) 9.0(12.6) 0.03(12.8)
4-3	PM2007 IHPV	1050 °C 400 MPa	1.1	5.9	Gl-Ol-Spl-Cpx-Pl-Q	Gl(3) Cpx(3) D-Cpx/L	254(18.8) 451(13.8) 1.8(23.4)
3-1	PM2007 IHPV	1092 °C 402 MPa	1.1	5.1	Gl-Ol-Spl-Q	Gl(10) Ol(3) Spl(3) D-Ol/L D-Spl/L	331(0.6) 6.7(8.8) 1078(15.6) 0.02(8.8) 3.3(15.6)
3-2	PM2007 IHPV	1092 °C 402 MPa	0.7	4.2	Gl-Ol-Spl-Cpx-Q	Gl(10) Ol(3) D-Ol/L	298(11.8) 9.6(10.0) 0.03(15.4)
6-1	PM2007 IHPV	1155 °C 415 MPa	0.8	4.2	Gl-Ol-Spl-Q	Gl(8) Ol(3) D-Ol/L	310(0.6) 12.70(13.2) 0.041(13.2)
7-2	PM2007 IHPV	1198 °C 420 MPa	2.9	4.7	Gl-Ol-Spl-Q	Gl(12) Ol(5) D-Ol/L	284.4(1.4) 1.86(13.8) 0.007(13.9)
7-3	PM2007 IHPV	1198 °C 420 MPa	2.1	2.3	Gl-Ol-Spl-Q	Gl(9) Ol(8) Sp(4) D-Ol/L D-Spl/L	295.4(0.6) 5.64(16.0) 553(22.0) 0.019(16.0) 1.9(22.0)
PCW11	P2002 PC	1160 °C 1500 MPa	3.5	5.8	Gl-Cpx-Opx-Spl-Q	Gl(8) Cpx(3) D-Cpx/L	369(1.2) 128(6.0) 0.3(6.2)
PCW12	P2002 PC	1180 °C 1450 MPa	2.3	3.7	Gl-Ol-Spl-Q	Gl(9) Ol(3) Sp(3) D-Ol/L D-Spl/L	286(0.6) 2.74(39.0) 323(6.0) 0.010(39.0) 1.1(6.0)
PCW13	P2002 PC	1180 °C 950 MPa	3.1	5.0	Gl-Ol-Spl-Q	Gl(7) Ol(7) D-Ol/L	288(1.8) 1.74(13.4) 0.006(13.6)

Gl=glass, Ol=olivine, Spl=spinel, Cpx=clinopyroxene, Opx=orthopyroxene, Pl=plagioclase, Q=quench crystals, L=liquid, D-Ol/L=olivine-liquid partition coefficient; n=number of averaged analyses. Ref.=reference; Exp.=experiment; Temp.=temperature; Press.=pressure; P2002=Pichavant et al. 2002; PM2007=Pichavant & Macdonald 2007; IHPV=internally heated pressure vessel experiment; PC=piston cyclinder experiment; uncertainties on compositions are given as two relative standard deviations (2RSD%). The reported fO_2 values are expressed relative to the QFM buffer defined by O'Neill (1987) in log bar units.

Table 2: Regression parameters for equation 1 and 2 olivine-melt V oxybarometers

Equation 1	Coeff.	Error	Probability		
Constant	-3.2848	0.1670	3.4955E-25	R^2	0.94
Log(D_V)	-2.9893	0.1075	4.4346E-32	Observations	52
				Regressions	1
Equation 2	Coeff	Error	Probability		
Constant	-2.8438	0.1261	1.5999E-27	R^2	0.97
Log(D_V)	-3.1960	0.0772	8.8955E-40	Observations	52
h-NBO/T	-0.8781	0.1127	3.9404E-10	Regressions	2

D_v is the V partitioning coefficient for olivine-melt; h-NBO/T is the hydrous NBO/T, calculated as outlines in the text. Coeff.=Coefficients of the regression. Uncertainties can be calculated as

Table 3: Estimated range of possible melt compositions and calculated mineral-melt partitioning coefficients for the STV301 magma during intermittent crustal storage

	Early-stage storage[a]			Late-stage storage[b]		
Estimate	E1	E2*	E3*	E4	E5*	E6*
	Bulk rock	Exp. glass	Calc. melt	Calc. melt	Exp. glass	Matrix
SiO_2	45.0(0.8)	45.9(0.4)	45.8(0.9)	48.0(1.7)	47.0(0.5)	45.5(1.4)
TiO_2	1.1(0.6)	1.0(0.1)	1.1(0.6)	1.3(0.2)	1.2(0.1)	0.7(0.3)
Al_2O_3	14.7(0.4)	15.0(0.4)	15.7(0.6)	18.8(1.8)	17.4(0.2)	20.6(4.3)
Fe_2O_3[d]	3.0(0.2)	3.1(0.2)	2.9(0.3)	2.7(0.5)	2.9(0.1)	2.7(1.8)
FeO[d]	6.3(0.4)	6.4(0.3)	6.0(0.5)	4.9(0.9)	5.6(0.2)	5.0(3.2)
MnO	0.2(0.1)	0.1(0.1)	0.2(0.1)	0.2(0.1)	0.2(0.1)	0.1(0.1)
MgO	11.5(0.2)	10.2(0.6)	9.3(0.7)	3.8(2.9)	6.4(0.2)	5.3(2.0)
CaO	10.5(0.2)	11.0(0.4)	11.1(0.3)	11.7(0.6)	11.3(0.2)	11.7(1.8)
Na_2O	2.2(0.1)	2.2(0.2)	2.3(0.1)	3.0(0.4)	2.5(0.1)	2.8(0.5)
K_2O	0.5(0.1)	0.5(0.1)	0.5(0.1)	0.7(0.2)	0.6(0.1)	0.6(0.1)
H_2O[c]	5.0(1.0)	5.0(1.0)	5.0(1.0)	5.0(1.0)	5.0(1.0)	5.0(1.0)
V	284(3)	284(4)	291(5)	285(7)	315(19)	283(92)
Sc	42.0(0.9)	44.0(1.0)	41.5(1.0)	31.1(4.1)	40.9(2.5)	39.8(17.8)
Y	14.4(0.3)	14.1(0.4)	14.8(0.7)	17.8(1.7)	16.0(1.7)	17.1(2.5)
Ni	340(5.0)	177(2.3)	228(29)	87(99)	89(14)	77(39)
NBO/T	0.81	0.74	0.70	0.37	0.50	0.40
h-NBO/T	1.32	1.24	1.20	0.82	0.97	0.86
K_DOl/L(FeT-Mg)	0.27	0.24	0.23	0.16	0.25	0.23
K_DOl/L(V)	0.014-0.020	0.014-0.020	0.014-0.019	0.015-0.018	0.013-0.016	0.015-0.018
K_DOl/L(Sc/Y)	26-44	24-41	27-46	45-79	31-54	34-59
K_DOl/L(Ni)	5.2-7.6	10-15	7.8-11	16-23	15-22	18-26
K_DSpl/L(V)	-	-	-	2.9-3.3	2.8-3.1	3.1-3.4

Concentrations nomalized to 100 wt% for major and minor oxide components including H_2O and in ppm for trace elements V, Sc, Y, and Ni with estimated uncertainties (2std) in parentheses. a=Estimated early-stage storage melt compositions (E1 to E3) and calculated partitioning coefficients for primitive olivine phenocryts cores (~Fo89, ~4.0-5.6 ppm V, ~5.7-7.4 ppm Sc, ~0.06-0.08 ppm Y, ~1780-2590 ppm Ni). b=Estimated late-stage storage melt compositions (E4 to E6) and calculated partitioning coefficients for evolved olivine phenocryst cores (~Fo84-86, ~4.2-5.1 ppm V, ~5.8-8.0 ppm Sc, ~0.04-0.10 ppm Y, ~1350-2000 ppm N) and spinel cores (>Mg#40, ~870-970 ppm V). c=estimated following Pichavant & Macdonald (2007). d=estimated using the formulation of Kress & Carmichael (1991) with fO_2 constrained using our equation 1 oxybarometer. (E1) Bulk-rock sample, which was analyzed as a glass fused from STV301 rock powder, which was the experimental starting material for the STV301 experiments. Oxide concentrations are from PM2007. (E2) Experimental glass composition 7-2. Oxide concentrations are from PM2007. (E3) Bulk-rock composition minus xenocryst and primtive phenocryst core compositions. (E4) Bulk-rock composition minus xenocryst and primtive to evolved phenocryst core compositions. (E5) Average of glass compositions 3-1 and 3-2. Oxide concentrations are from PM2007. (E6) Coarsely crystallized matrix composition. Indicated uncertainties for E1, E2, E4, and E5 are analytical uncertainties; indicated uncertainties for E3 and E6 are analytical uncertainties for bulk-rock composition plus and an estimated arbritrary uncertainty of ±20% on mineral proportions used for calculating residual melt composition. PM2007=Pichavant & Macdonald (2007). * Our best estimates. Additional details on the calculated melt compositions are provided in Tables S10 and S11.

Table 4: Calculated temperature (T) in °C and oxygen fugacity (fO_2) relative to ΔQFM in log units for the STV301 magma

Calibration		Early-stage storage				Late-stage storage			
		E1	E2*	E3*	**Av±σ(2sd)	E4	E5*	E6*	**Av±σ(2sd)
T_Ol/L_Sc/Y_MO2013	Av	1207	1220	1194	1209±30	1059	1044	1112	1078±30
	Max	1262	1276	1248		1104	1090	1161	
	Min	1151	1163	1139		1013	998	1063	
T_Ol/L_Ni_P2017	Av	1365	1207	1277	1242±60	1163	1144	1117	1130±60
	Max	1418	1250	1325		1206	1186	1157	
	Min	1312	1164	1229		1120	1102	1076	
fO_2_Ol/L_V_MO2013	Av	1.73	1.83	1.93	1.9±0.5	2.70	2.68	2.64	2.7±0.5
	Max	2.02	2.12	2.19		2.88	2.86	2.81	
	Min	1.43	1.53	1.66		2.52	2.50	2.46	
fO_2_Ol/L_V_W2019	Av	1.93	1.99	2.13	2.1±0.5	2.87	2.90	2.86	2.9±0.5
	Max	2.21	2.27	2.41		3.03	3.06	3.02	
	Min	1.64	1.70	1.85		2.71	2.74	2.69	
fO_2_Ol/L_V_S2018	Av	2.12	2.12	2.16	2.1±0.9	2.15	2.29	2.14	2.2±0.9
	Max	2.34	2.34	2.38		2.28	2.42	2.27	
	Min	1.89	1.89	1.93		2.02	2.16	2.01	
fO_2_Ol/L_V_Eqn1	Av	2.03	2.03	2.06	2.1±0.5	2.07	2.20	2.06	2.1±0.6
	Max	2.25	2.25	2.28		2.19	2.32	2.18	
	Min	1.81	1.81	1.84		1.94	2.07	1.93	
fO_2_Ol/L_V_Eqn2	Av	1.68	1.75	1.82	1.8±0.5	2.16	2.17	2.11	2.1±0.6
	Max	1.91	1.98	2.05		2.29	2.30	2.24	
	Min	1.45	1.52	1.59		2.02	2.03	1.98	
fO_2_Spl/L_V_W2019	Av	-	-	-	-	2.78	2.59	2.53	2.6±0.5
	Max	-	-	-		3.01	2.82	2.76	
	Min	-	-	-		2.54	2.35	2.29	

Temperatures were calculated using the Sc/Y thermometer of Mallmann & O'Neill (MO2013) and the Ni thermometer of Pu et al. (2017) (P2107). The fO_2 values were calculated using the oxybarometers of Mallmann & O'Neill (2013) (MO2013), Wang et al. (2019) (W2019), Shishkina et al. (2018) (S2018), and our new equation 1 and equation 2 oxybarometers. * Our best estimates; ** average for the best estimates E2 and E3 or E5 and E6, respectively. Reported uncertainties (σ at 2SD level) are inferred standard errors for M2013, W2019, and P2017, and calculated for S2018 and our calibrations. For Eqn 1 and 2, we have assumed errors of 0.001 (E1 to E3) and 0.002 (E4 to E5) on K_DOl/L(V) and errors of 0.1 (E1 to E3) and 0.2 (E4 to E5) on estimated hydrous melt NBO/T, following from the range of compositions presented in Table 3. L=liquid, Ol=olivine, Spl=spinel.